Chapter 21 MOLECULAR DYNAMICS METHOD FOR MICRO/NANO SYSTEMS

Shigeo Maruyama

Department of Mechanical Engineering, The University of Tokyo,

7-3-1 Hongo, Bunkyo-ku, Tokyo 113-8656, Japan

Phone: +81-3-5841-6421, Fax: +81-3-5800-6983,

E-mail: maruyama@photon.t.u-tokyo.ac.jp

http://www.photon.t.u-tokyo.ac.jp/

21.1. INTRODUCTION

Molecular dynamics simulations are becoming more important and more practical for microscale and nanoscale heat transfer problems. For example, studies of basic mechanisms of heat transfer such as phase change demand the understanding of microscopic liquid-solid contact phenomena. The efficient heat transfer at a three-phase interface (evaporation and condensation of liquid on a solid surface) becomes the singular problem in the macroscopic treatment. The nucleation theory of liquid droplets in vapor or of vapor bubbles in liquid sometimes needs to take account of nuclei of the size of molecular clusters. The effect of the surfactant on the heat and mass transfer through liquid-vapor interface is also an example of the direct effect of molecular scale phenomena on the macroscopic heat and mass transfer. Even though there has been much effort of extending our macroscopic analysis to extremely microscopic conditions in space (micrometer and nanometer scales), time (microseconds, nanoseconds and picoseconds), and rate (extremely high heat flux), there are certain limitations in the extrapolations. Hence, the bottom-up approach from molecular level is strongly anticipated.

On the other hand, recent advances in microscale and nanoscale heat transfer and in nanotechnology require the detailed understandings of phase change and heat and mass transfer in nanometer and micrometer scale regimes. The chemical engineering processes to generate nanoscale structures such as carbon nanotubes or mesoporous silica structures are examples. The wetting of liquid or absorption is also important since the adhesive force is extremely important for micro/nano system and the creation of extremely large surface area is possible with nanoscale structures. The use of molecular dynamics simulations is straightforward for such a nanoscale system. Here, again, it is important to compare such nanoscale phenomena with macroscopic phenomena, because an analogy to the macroscopic system is often an important strategy in understanding a nanoscale phenomenon. Important physics intrinsic to a nanoscale system is usually found through the rational comparison

with a macroscopic system. In this chapter, one of the promising numerical techniques, the classical molecular dynamics method, is overviewed with a special emphasis on applications to inter-phase and heat transfer problems. The molecular dynamics methods have long been used and are well developed as a tool in statistical mechanics and physical chemistry [1, 2]. However, it is a new challenge to extend the method to the spatial and temporal scales of macroscopic heat transfer phenomena [3-6]. On the other hand, the thin film technology related to the semiconductor industry and recent nanotechnology demands the prediction of heat transfer characteristics of nanometer scale materials [7, 8].

In addition to a brief description of the basic concept of molecular dynamics method; various examples of potential functions such as the Lennard-Jones potential for rare gas; effective pair potential for water, alcohols and organic molecules; many-body potential for silicon and carbon; and embedded atom potential for solid metals are discussed. Depending on the nature of electronic structure or simply the bonding characteristics, suitable choices of potential functions are extremely important for realistic simulations. Several examples of potential functions between heterogeneous systems are found such as between water-solid platinum, hydrogen-graphite (carbon nanotube), water-graphite (carbon nanotube) and metal-carbon. Various techniques to obtain thermodynamic and thermo-physical properties by equilibrium and non-equilibrium simulations are explained. Finally, predictions of thermal conductivity and the thermal boundary resistance between solid materials and solid-liquid interfaces are discussed.

Examples of various applications of molecular dynamics simulations follow. After the brief introduction to the liquid-vapor interface characteristics such as the surface tension and condensation coefficient, solid-liquid-vapor interaction characteristics such as liquid-contact phenomena and absorption phenomena will be discussed from molecular stand point. In addition to the simple Lennard-Jones system discussed in a previous review [3], a simulation of liquid water droplets in contact with a platinum solid surface is introduced. Because water molecules make hydrogen bonds,

the contact phenomena are drastically different from the simple Lennard-Jones fluid. The water droplet exhibits a finite contact angle on the absorbed monolayer of water film. The contact angle is determined by the surface energy between this monolayer water film and bulk liquid-water film. Topics in nucleation and phase change phenomena include homogeneous nucleation of liquid droplets for a Lennard-Jones fluid and water and heterogeneous nucleation of liquid droplets and vapor bubbles on a solid surface for a simple Lennard-Jones fluid. Here a critical discussion of the modification of classical nucleation theory for small confined system is addressed. Especially for vapor bubble nucleation, the compression of a confined liquid results a large modification of the free energy dependence on bubble radius. In addition, an example of a crystallization process of amorphous silicon is discussed. The nucleation process of molecules such as fullerenes and single-walled carbon nanotubes (SWNTs) are also discussed as the connection to nanotechnology.

Finally, the nanoscale heat transfer problem related with carbon nanotubes is discussed. After the brief introduction to carbon nanotubes, interaction of nanotubes with fluids such as the hydrogen-absorption problem and water-nanotube interactions are discussed. Then, the molecular dynamics prediction of thermal conductivity along a nanotube and thermal boundary resistance with various environments are discussed.

21.2. MOLECULAR DYNAMICS METHOD

Knowledge of statistical mechanical gas dynamics has been helpful to understand the relationship between molecular motion and macroscopic gas dynamics phenomena [9]. Recently, a direct simulation method using the Monte Carlo technique (DSMC) developed by Bird [10] has been widely used for the practical simulations of rarefied gas dynamics. On the other hand, statistical mechanical treatment of solid-state matters has been well developed as solid state physics [e.g., 11]. For example, the direct simulation of the Boltzmann equation of phonon dynamics is being developed

and applied to the heat conduction analysis of thin films [12, 13] or nanowires [14]. Here, molecular dynamics simulations are expected to directly address phonon-phonon and phonon-boundary scattering models. Furthermore, when we need to take care of liquid or inter-phase phenomenon, which is inevitable for phase-change heat transfer, the statistical mechanics approach is not as developed as for the gas-dynamics or the solid-state statistics. The most powerful tool for the investigation of the microscopic phenomena in heat transfer is the molecular dynamics method [e.g, 1-6]. In principal, the molecular dynamics method can be applied to all phases of gas, liquid, and solid and to interfaces of these three phases.

21.2.1 Equations of Motion and Potential Functions

In the classical molecular dynamics method, the equations of motion (Newton's equations) are solved for atoms as

$$m_i \frac{d^2 \mathbf{r}_i}{dt^2} = \mathbf{F}_i = -\nabla_i \Phi , \qquad (21.1)$$

where m_i, r_i and F_i are the mass, position vector and force vector of molecule i, respectively. Φ is the potential of the system. This classical form of the equation of motion is known to be a good approximation of the Schrödinger equation when the mass of atom is not too small and the system temperature is high enough compared with the gap of quantum energy levels associated with the dynamics. For translational and rotational motions of molecules, Eq. (21.1) can be valid except for light molecules such as hydrogen and helium and except at cryogenetic temperatures. On the other hand, some quantum corrections are sometimes essential for intra-molecule vibrational motion of small molecules even at room temperature. Once the potential of a system is obtained, it is straightforward to numerically solve Eq. (21.1). In principal, any of gas, liquid, solid states, and inter-phase phenomena can be solved without the knowledge of "thermo-physical properties" such as thermal conductivity, viscosity, latent heat, saturation temperature and surface tension.

The potential of a system $\Phi(\mathbf{r}_1, \mathbf{r}_2, ...\mathbf{r}_N)$ can often be reasonably assumed to be the sum of the effective pair potentials $\phi(r_{ij})$ as

$$\Phi = \sum_i \sum_{j>i} \phi(r_{ij}), \qquad (21.2)$$

where r_{ij} is the distance between molecules *i* and *j*. It should be noted that the effective pair potential approximation in Eq. (21.2) is convenient for simple potential systems but cannot be applied for complex potentials such as silicon and carbon. In the following examples of the potential functions for covalent systems such as carbon and silicon and for the embedded atom model for solid metals, this approximation is not used.

21.2.2 Examples of Potential Functions

The determination of the suitable potential function is extremely important for a molecular dynamics simulation. Here, the well-known Lennard-Jones potential for van der Waals interactions, potential forms for water and larger molecules, multi-body potentials for silicon and carbon, and embedded atom models for solid metals are briefly reviewed.

Lennard-Jones Potential

The most widely used pair potential for molecular dynamics simulations is the Lennard-Jones (12-6) potential function expressed as

$$\phi(r) = 4\varepsilon\left[\left(\frac{\sigma}{r}\right)^{12} - \left(\frac{\sigma}{r}\right)^{6}\right], \qquad (21.3)$$

where ε and σ are energy and length scales, respectively, and *r* is the intermolecular distance as shown in Fig. 21.1. The intermolecular potential of inert monatomic molecules such as Ne, Ar, Kr and Xe is

known to be reasonably expressed by this function with the parameters listed in Table 21.1. Moreover, many studies in computational and statistical mechanics have been performed with this potential as the model potential. Here, the equation of motion can be non-dimensionalized by choosing σ, ε and m as length, energy and mass scale, respectively. The reduced formulas for typical physical properties are listed in Table 21.2. When a simulation system consists of only Lennard-Jones molecules, the non-dimensional analysis has an advantage of generality over analysis made with the dimensional model. Then, molecules are called Lennard-Jones molecules, and argon parameters $\sigma = 0.34$ nm, $\varepsilon = 1.67 \times 10^{-21}$ J, and $\tau = 2.2 \times 10^{-12}$ s are often used to describe dimensional values in order to illustrate the physical meaning. The phase-diagram of a Lennard-Jones system [15, 16] is useful for designing a simulation. An example of the phase-diagram using the equations by Nicolas et al. [15] is shown in Fig. 21.2. Here, the critical and triplet temperatures are $T_c^* = 1.35$ and $T_t^* = 0.68$, or $T_c = 163$ K and $T_t = 82$ K with argon properties [17].

For the practical simulation, the Lennard-Jones function in Eq. (21.3) is cutoff at the intermolecular distance $r_C = 2.5\sigma$ to 5.5σ. In order to reduce the discontinuity at the cut-off point, several forms of smooth connection have been proposed (for instance [18]). However, for pressure or stress calculations, a contribution to the properties from far away molecules with modified potentials can result in a considerable error as demonstrated for surface tension [19]. Since the modification of the potential makes the long-range correction too complex, the simple cut-off strategy may be advantageous.

Effective Pair Potential for Water

The effective pair potential form for water has been intensively studied. The simple form of SPC (Simple Point Charge) [20] and SPC/E (Extended SPC) [21] potentials were introduced by Berendsen et al. SPC/E potentials employ the rigid water configuration in Fig. 21.3. Here, the

negative point charge is on the oxygen atom with the distance of OH just 0.1 nm and the angle of HOH the tetrahedral angle $\theta_t = 2\cos^{-1}\left(1/\sqrt{3}\right) \cong 109.47°$. The effective pair potential of molecules at R_1 and R_2 are expressed as the superposition of Lennard-Jones functions of oxygen-oxygen interactions and the electrostatic potential by charges on oxygen and hydrogen as follows.

$$\phi_{12} = 4\varepsilon_{OO}\left[\left(\frac{\sigma_{OO}}{R_{12}}\right)^{12} - \left(\frac{\sigma_{OO}}{R_{12}}\right)^{6}\right] + \sum_i \sum_j \frac{q_i q_j e^2}{4\pi\varepsilon_0 r_{ij}}, \quad (21.4)$$

where R_{12} represents the distance of oxygen atoms, and σ_{OO} and ε_{OO} are Lennard-Jones parameters. The Coulombic interaction is the sum of nine pairs of point charges.

TIP4P potential proposed by Jorgensen et al. [22] employed the structure of water molecule as r_{OH} = 0.09572 nm and ∠HOH = 104.52° based on the experimentally assigned value for the isolated molecule. The positive point charges q were on hydrogen atoms, and the negative charge $-2q$ was set at a distance r_{OM} from the oxygen atom on the bisector of the HOH angle, as in Fig. 21.3. The potential parameters of SPC/E and TIP4P listed in Table 21.3 were optimized for thermodynamic data such as density, potential energy, specific heat, evaporation energy, self-diffusion coefficient, thermal conductivity, and structure data such as the radial distribution function and neutron diffraction results at 25 °C and 1 atm. This potential is regarded as one of the OPLS (optimized potential for liquid simulations) set covering liquid alcohols and other molecules with hydroxyl groups developed by Jorgensen [23].

Carravetta-Clementi (CC) potentials [24] were based on *ab initio* quantum molecular calculations of water dimer with the elaborate treatment of electron correlation energy. The assumed structure and the distribution of charges are the same as for TIP4P as shown in Fig. 21.3 with a different length r_{OM} and amount of charge. For CC potentials, the interaction of molecules is parameterized as a complex form [24]. Among these rigid water models, SPC/E, TIP4P and CC potentials are well accepted in recent simulations of liquid water including the demonstration of the excellent agreement of surface tension with experimental results using the SPC/E potential [25].

Because all of these rigid water models are “effective” pair potentials optimized for liquid water, it must be always questioned if they are applicable to small clusters or liquid-vapor interfaces. Even though the experimental permanent dipole moment of isolated water is 1.85 D, most rigid models employ higher values such as 2.351 D for SPC/E to effectively model the induced dipole moment at liquid phase. The direct inclusion of the polarizability to the water models results in the many-body potential, which requires the iterative calculation of polarization depending on surrounding molecules. The polarizable potential forms derived from TIP4P [26, 27], MCY [28] and SPC [29] are used to simulate the structure of small clusters and transition of monomer to bulk properties.

Potential for Larger Molecules in Liquid Phase (OPLS and AMBER)

For alcohol [23] and other larger hydrocarbon molecules with hydroxyl groups [30], the OPLS (optimized potential for liquid simulation) potential developed by Jorgensen is widely used. As mentioned in the previous section, TIP4P for water is one of the potentials of this collection. As in the case of water molecule, hydrogen atoms are not explicitly modeled but methyl and methylene units are treated as pseudo-atoms. All bond lengths are rigidly constrained to their equilibrium values. Methyl and methylene groups are labeled C_1 through C_n from the tail group, i.e., methyl group, to the head group, i.e., hydroxyl group. The interaction potential E_{AB} between two molecules A and B is determined by the summation of Coulomb and Lennard-Jones interactions between all intermolecular pairs of sites as follows.

$$E_{AB} = \sum_{i}^{A} \sum_{j}^{B} \left[4\varepsilon_{ij} \left[\left(\frac{\sigma_{ij}}{r_{ij}} \right)^{12} - \left(\frac{\sigma_{ij}}{r_{ij}} \right)^{6} \right] + \frac{q_i q_j e^2}{4\pi\varepsilon_0 r_{ij}} \right] \qquad (21.5)$$

where q_i and q_j are the partial charges on united pseudo-atoms i and j, r_{ij} is the distance between these atoms. Because of all pairs of interaction of the Lennard-Jones term, Equation (21.5) is a little more complex than equation (21.4) for TIP4P water.

In order to obtain the Lennard-Jones potential parameters σ_{ij} and ε_{ij} for variety of combinations of molecules, the well known combination rule [31] is used as follows.

$$\sigma_{ij} = (\sigma_{ii} + \sigma_{jj})/2 \quad (21.6)$$

$$\varepsilon_{ij} = \sqrt{\varepsilon_{ii}\varepsilon_{jj}} \quad (21.7)$$

This combination rule is often used for obtaining Lennard-Jones parameter of unknown combinations.

The potential field for larger organic molecules and biological molecules such as proteins and nucleic acids are much more complicated. The force field parameters obtained from molecular mechanics and accurate ab initio calculations are summarized as AMBER force field by Kollman et al. [32-34]. Cornell et al. [33] used the following additive potential form.

$$E_{\text{pair}} = \sum_{\text{bonds}} K_r (r - r_{eq})^2 + \sum_{\text{angles}} K_\theta (\theta - \theta_{eq})^2 + \sum_{\text{dihedrals}} \frac{1}{2} V_n \left[1 + \cos(n\phi - \gamma)\right] + \sum_{\text{van der Waals}}^{i<j} \left(\frac{A_{ij}}{R_{ij}^{12}} - \frac{B_{ij}}{R_{ij}^{6}} \right) + \sum_{\text{electrostatic}}^{i<j} \left(\frac{q_i q_j}{4\pi\varepsilon R_{ij}} \right), \quad (21.8)$$

with the bonds and angles represented by a simple diagonal harmonic expression, the van der Waals interaction represented by a Lennard-Jones potential, electrostatic interactions modeled by a Coulombic interaction of atom-centered point charges, and dihedral energies represented with a simple set of parameters. Electrostatic and van der Waals interactions are only calculated between atoms in different molecules or for atoms in the same molecule separated by at least three bonds. The molecular dynamics simulation code also called AMBER implementing these force fields is also developed by Kollman's group [35].

Many-Body Potential for Carbon and Silicon

The pair-potential approximation cannot be used for atoms with covalent chemical bonds such as silicon and carbon. SW potentials for silicon crystal proposed by Stillinger and Weber in 1985

[36] was made of a two-body term and a three-body term that stabilizes the diamond structure of silicon. This old potential is still widely used because this potential accurately describes elastic properties, phonon dispersion relations, melting point, yield strength and thermal expansion coefficients. Tersoff [37-39] proposed a many-body potential function for silicon, carbon, germanium and combinations of these atoms. The Tersoff potential [38] is widely used for simulations of solid silicon. Brenner modified the Tersoff potential for carbon and extended it for a hydrocarbon system [40]. A simplified form of Brenner potential removing rather complicated 'conjugate terms' is widely used for studies of fullerene [41] and carbon-nanotubes. Both the Tersoff potential and the simplified Brenner potential can be expressed as following in a unified form [3]. The total potential energy of a system is expressed as the sum of every chemical bond as

$$\Phi = \sum_i \sum_{j(i<j)} f_C(r_{ij}) \left\{ V_R(r_{ij}) - b^*_{ij} V_A(r_{ij}) \right\}, \quad (21.9)$$

where the summation is for every chemical bond. $V_R(r)$ and $V_A(r)$ are repulsive and attractive parts of the Morse type potential, respectively.

$$V_R(r) = f_C(r) \frac{D_e}{S-1} \exp\left\{ -\beta\sqrt{2S}\left(r - R_e\right) \right\} \quad (21.10)$$

$$V_A(r) = f_C(r) \frac{D_e S}{S-1} \exp\left\{ -\beta\sqrt{2/S}\left(r - R_e\right) \right\} \quad (21.11)$$

The cutoff function $f_C(r)$ is a simple decaying function centered at $r = R$ with the half width of D.

$$f_C(r) = \begin{cases} 1 & (r < R - D) \\ \frac{1}{2} - \frac{1}{2}\sin\left[\frac{\pi}{2}(r - R)/D \right] & (R - D < r < R + D) \\ 0 & (r > R + D) \end{cases} \quad (21.12)$$

Finally, the b^*_{ij} term of Eq.(21.9) expresses the modification of the attractive force $V_A(r)$ depending on θ_{ijk} and the bond angle between bonds *i*-*j* and *i*-*k*.

$$b^*_{ij} = \frac{b_{ij} + b_{ji}}{2}, \quad b_{ij} = \left(1 + a^n \left\{ \sum_{k(\neq i,j)} f_C(r_{ik}) g(\theta_{ijk}) \right\}^n \right)^{-\delta} \quad (21.13)$$

$$g(\theta) = 1 + \frac{c^2}{d^2} - \frac{c^2}{d^2 + (h - \cos\theta)^2} \qquad (21.14)$$

Parameter constants for Tersoff potentials for silicon (improved elastic properties) [38] and carbon and Brenner potentials for carbon are listed in Table 21.4. See more discussions in the previous review [3].

Recently, a modified 'second generation empirical bond order potential' for carbon was developed by Brenner et al. [42]. A significantly better description of bond energies, lengths, and force constants as well as elastic properties is achieved with a single parameter set.

Pair Potential and the Embedded Atom Method (EAM) for Solid Metal

For solid metal crystals, several physical properties can be used to fit to the pair potential functions such as Morse potential and Johnson potentials. The Morse potential is expressed as

$$\phi(r) = D_e\left[\exp\{-2\beta(r - R_e)\} - 2\exp\{-\beta(r - R_e)\}\right] \quad (21.15)$$

where D_e, R_e and β are dissociation energy, equilibrium bond length and a constant with dimensions of reciprocal distance, respectively. This form of Eq. (21.15) corresponds to the special case of $S = 2$ in the generalized Morse-type functions in Eq. (21.10) and (21.11). The parameters calculated by Girifalco & Weizer [43] with energy of vaporization, the lattice constant and the compressibility for cubic metals (fcc and bcc) can predict reasonable elastic constants [43]. See Table 5 of the previous review [4].

For calculations involving solid metals and alloys, it is well known that such pair potential functions are far from satisfactory when system is not the perfect crystal [44]. When some surface or interface defects are included, pair potential functions that are independent of coordination cannot reproduce the realistic potential field. The angle dependence of potential is, in general, not as critical as in the covalent cases such as carbon and silicon because *d*-orbital electrons are a little more flexible.

In contrast with the “bond order concept” for covalent atoms, the following ‘Embedded Atom Method’ (EAM) was suggested and developed by Daw and Baskes [45-48] as a way to overcome the main problem with two-body potentials. The basic concept for EAM is that the potential energy can be calculated by embedding each atom to the electric field made of all other atoms. Later, ‘Modified Embedded Atom Method’ (MEAM) was also developed by Baskes group [49-52]. Here, the bond-angle was explicitly handled and the possibility to extend the application range to covalent system such as silicon was explored. It should be noted that ideas of electron density and density functional theory (DFT) are discussed in the formulation of the EAM and MEAM, however, they are classical potential functions and no quantum dynamics equation is solved when using the potential functions. See the previous review [4] for a more detailed summary.

Finally, it should be noted that solid metals are always problematic for heat conduction problems due to the luck of the effective technique to handle free electrons in conjunction to molecular dynamics framework.

21.2.3 Integration of the Newtonian Equation

The integration of the equation of motion is straightforward. Unlike the simulation of fluid dynamics, a simpler integration scheme is usually preferred. Verlet’s leap-frog method shown below is widely used in practical simulations [1]. After the velocity of each molecule is calculated as Eq. (21.16), positions are updated in Eq. (21.17).

$$\mathbf{v}_i\left(t+\frac{\Delta t}{2}\right)=\mathbf{v}_i\left(t-\frac{\Delta t}{2}\right)+\Delta t\frac{\mathbf{F}_i(t)}{m_i} \qquad (21.16)$$

$$\mathbf{r}_i(t+\Delta t)=\mathbf{r}_i(t)+\Delta t\mathbf{v}_i\left(t+\frac{\Delta t}{2}\right) \qquad (21.17)$$

A typical time step Δt is about 0.005 τ or 10 fs with argon property of Lennard-Jones potential. More elaborate integration schemes such as Gear’s predictor-corrector method [1] are sometimes employed

depending on the complexity of the potential function and the demand for the accuracy of motion at each time step.

Although the principal equation to solve is Eq. (21.1), classical rotational equations have to be solved for rigid small molecules with such as rigid water potential. The equation is the classical rotation equation of motion [1]. On the other hand, for large molecules expressed with such methods as OPLS and AMBER potentials need to be solved with the constraint dynamics, if the bond length is fixed. For such constraint dynamics, the efficient SHAKE algorism [1] is often used.

21.2.4 Boundary Conditions: Spatial and Temporal Scales

Since the spatial and temporal scales handled with the molecular dynamics method is extremely small compared to the scale of the normal microscopic heat transfer problems, the most important points of the design of a molecular dynamics simulation are the boundary conditions. Many molecular dynamics simulations have used the fully periodic boundary condition, which assumes that the system is simply homogeneous for an infinite length scale. The implementation of the periodic boundary condition is very simple. Any information beyond a boundary can be calculated with the replica of molecules. The interactions of molecules are calculated beyond the periodic boundary with replica molecules. In order to avoid the calculation of potential between a molecule and its own replica, the potential must be cutoff at a distance smaller than half the width of the base-cell scale. This is not a serious problem for the short-range force such as Lennard-Jones potential, which decays as r^{-6}. On the contrary, since Coulombic potential decays only with r^{-1}, the simple cutoff is not possible. Usually, the well-known Ewald sum method [1] is employed, where the contribution from molecules in replica cells is approximated by a sophisticated manner.

Many problems in heat transfer may include a phenomenon with a larger scale than the calculation domain, such as relatively large photon mean free path, instability with large wavelength

or a large modulation of properties. The difficulty in the boundary condition is less for gas-phase molecules because the contribution of potential energy compared to kinetic energy is small. If the potential contribution is ignored, some simple boundary condition such as mirror reflection boundaries can be used by simply changing the velocity component as if a molecule makes an inelastic reflection. When it is impossible to use the periodic boundary condition, a solid wall or a vapor layer can be connected in the realistic fashion. Then, the appearance of a new 'interface' leads to a significant change of the physics. Several different levels of the solid boundary conditions are discussed in detail in the previous review [3].

21.2.5 Initial Conditions and Control of Temperature and/or Pressure

The initial condition for each molecule is usually assigned by giving the velocity $v = \sqrt{3k_B T_C / m}$ with random directions for all monatomic molecules. The Maxwell-Boltzmann velocity distribution can be obtained after some equilibration calculations. The equilibrium system can often be calculated for constant temperature and constant pressure conditions. The simple temperature control of the equilibrium system can be realized by just scaling the velocity of molecules as $v_i' = v_i \sqrt{T_C / T}$ with the current temperature T and the desired temperature T_C. Remember that this control has to be applied in many steps because of the relaxation of potential energy. More elaborate techniques to realize the constant temperature system are known as the Anderson method [53] and the Nosé-Hoover method [54, 55].

Anderson method mimics random collisions with an imaginary heat bath particle. At intervals, the velocity of a randomly selected molecule is changed to a value chosen from the Maxwell-Boltzmann distribution. The choice of this interval has a significant influence on the result.
The Nosé-Hoover thermostat method involves modifying of the equation of motion as

$$m_i \frac{d^2\mathbf{r}_i}{dt^2} = \mathbf{F}_i - \zeta m_i \frac{d\mathbf{r}_i}{dt}, \quad \frac{d\zeta}{dt} = \frac{2\left(E_k - E_k^{\,0}\right)}{Q} \qquad (21.18)$$

where ζ is the friction coefficient, E_k is kinetic energy of the system, E_{k0} is kinetic energy corresponding to the desired temperature T_C, and Q is the thermal inertia parameter. All of these constant temperature techniques have been probed to give a statistically correct canonical ensemble, but the physical meaning of the velocity re-scaling is not clear.

Andersen [53] described a technique to realize the constant pressure simulation. The simulation box size V is altered similar to the action of a piston with a mass. Parrinello and Rahman [56, 57] extended this technique to change the simulation box shape as well as size for solid crystal. Berendsen [58] proposed a very simple "pressure bath" technique for the constant pressure simulation. The system pressure obeys

$$dP/dt = (P_C - P)/t_P \qquad (21.19)$$

by scaling the box size and position of molecules by a factor $\chi^{1/3}$ at each step.

$$\mathbf{r}' = \chi^{1/3}\mathbf{r}, \quad \chi = 1 - \beta_T \frac{\Delta t}{t_p}\left(P_C - P\right), \qquad (21.20)$$

where β_T, t_p are the isothermal compressibility and time constant parameter, respectively.

Finally, it should be stressed again that all of these techniques to realize constant temperature or constant pressure are artificial and are used to reproduce the statistical ensemble. The physical meaning of the modification of position or velocity of each molecule is not clear.

21.2.6 Thermophysical and Dynamic Properties

Molecular motion can be related to the thermodynamics properties through the entropy S defined as

$$S = k_B \ln \Omega \qquad (21.21)$$

where Ω is the phase-space volume. The statistical mechanical discussions for the microcanonical ensemble system (NVE ensemble), which is the ‘molecular dynamics’ ensemble, are fully described in Haile’s textbook [2]. As the final result, the thermodynamics temperature for monatomic molecules is simple expressed as the kinetic energy of molecules.

$$T = \frac{1}{3Nk_{\mathrm{B}}}\left\langle \sum_{i=1}^{N} m_i v_i^{\,2} \right\rangle \qquad (21.22)$$

The internal energy is the combination of kinetic and potential energies.

$$U = \frac{3}{2}Nk_{\mathrm{B}}T + \left\langle \sum_i \sum_{j>i} \phi(\mathbf{r}_{ij}) \right\rangle \quad (21.23)$$

The pressure is defined through the virial theorem as follows.

$$P = \frac{N}{V}k_{\mathrm{B}}T - \frac{1}{3V}\left\langle \sum_i \sum_{j>i} \frac{\partial \phi}{\partial \mathbf{r}_{ij}} \cdot \mathbf{r}_{ij} \right\rangle \qquad (21.24)$$

There is no simple technique to measure entropy and free energy directly by the molecular dynamics method. They cannot be defined as the time averages of phase-space trajectories, but are related to the phase-space volume [2]. The thermodynamics integration or test particle method is employed [2]. These properties are often obtained by the statistical Monte Carlo method.

Even though the potential energy and pressure for a homogeneous fluid can be calculated for relatively small system, there is an important consideration for practical calculation. Since potential energy and pressure are affected from quite long-range distances, it is convenient to consider the potential cut-off corrections. The ‘long-range correction’ techniques can be found in the previous review [4].

21.2.7 Heat Conduction and Heat Transfer

The thermal conductivity of homogeneous material can be calculated by three different

techniques of molecular dynamics: (1) equilibrium molecular dynamics with the Green-Kubo's formula, (2) non-equilibrium molecular dynamics (NEMD) developed by Evens [58, 59], and (3) non-equilibrium molecular dynamics with direct temperature differences. It should be noted that sometime both methods (2) and (3) are called 'non-equilibrium' molecular dynamics. For a homogeneous system, all of these simulations should give the same thermal conductivity with adequate simulation conditions [61, 62].

The simulation of heat conduction does not always involve simple calculations using thermal conductivity. The validity of Fourier's law in an extremely microscopic system such as thin films can only be examined by the direct non-equilibrium heat conduction calculation. The mechanism of heat conduction itself is also interesting [63, 64]. The heat flux through a volume is calculated as

$$\mathbf{q} = \frac{1}{2V}\left[\sum_{i}^{N} m_i v_i^{\,2}\mathbf{v}_i + \sum_{i}^{N}\sum_{j\neq i}^{N}\phi_{ij}\mathbf{v}_i - \sum_{i}^{N}\sum_{j\neq i}^{N}\left(\mathbf{r}_{ij}\mathbf{f}_{ij}\right)\mathbf{v}_i\right] \quad (21.25)$$

where the first and second terms related to summations of kinetic and potential energies carried by a molecule *i*. The third term, the tensor product of vectors $\boldsymbol{r}_{ij}$ and $\boldsymbol{f}_{ij}$, represents the energy transfer by the pressure work. Because of the third term, the calculation of heat flux is not trivial at all.

Thermal Conductivity of Solids

Since most direct heat transfer problems of micro/nano scale are currently related with thermophysical properties of solid materials, the heat conduction behavior of micro- and nano-devices are very much of importance. Simulations of thermal conductivity by the Boltzmann equation of phonon dynamics is being developed and applied to the heat conduction analysis of thin films [12, 13] or nanowires [14]. Here, the direct calculations of phonon dispersion relations, phonon mean free paths, and phonon scattering rates using the molecular dynamics simulations are anticipated [65-68].

The non-Fourier heat conduction problems should also be addressed by molecular dynamics simulations [69]. A good review of simulation of heat conduction problems in micro/nano scale solid can be found in reference [8].

Thermal Boundary Resistance

The thermal boundary resistance between solid crystals or at a solid and liquid interface becomes important for small systems. Here, it should be noted that the thermal boundary resistance does exist between epitaxially grown interfaces of solids or even solid-liquid interfaces [70-72]. The reduction of thermal conductivity by the super-lattice [73] is an excellent example of the importance of thermal boundary resistance. The direct molecular dynamics simulation of the thermal boundary resistance and the temperature jump across liquid-solid interfaces can be demonstrated in a simple simulation system [70]. When a constant heat flux is applied across the liquid-solid interface, a distinctive temperature jump near the solid-liquid interface can be observed. The thermal boundary resistance R_T is determined from the temperature jump T_{JUMP} and the heat flux q_W as $R_T = T_{JUMP} / q_W$. This thermal boundary resistance of that investigation was equivalent to a 5~20 nm thickness layer of liquid, and hence, is important only for such a small system. Direct experimental measurements of thermal boundary resistance and relevant molecular dynamics simulations are discussed for carbon nanotube-fluid system in a later section.

Matsumoto et al. [74] studied the thermal resistance between Lennard-Jones solid crystals by direct non-equilibrium molecular dynamics. Inside an fcc crystal, one-dimensional steady heat conduction was realized using a pair of temperature controlling heat baths. Four types of atomically continuous solid-solid interfaces were investigated: (1) crystals with different masses, (2) crystals with different interaction parameters, (3) crystals with various surface interaction parameters, and (4) crystals with different size parameters. Except for the case (4), the observed temperature profiles had

a discontinuity at the interface, from which the temperature jump was measured. The reduction of heat flux due to the temperature jump was larger than that predicted with a simple acoustic model. With similar molecular dynamics simulations of Lennard-Jones crystals, the thermal boundary resistance was modeled through the energy reflection rate [75]. Ohara et al. have analyzed the possible explanation of the thermal boundary resistance [71] based on an “intermolecular energy transfer” concept developed by the detailed studies of heat conduction in liquid phase water [63] and a Lennard-Jones fluid [64].

21.3. MOLECULAR DYNAMICS OF PHASE-INTERFACE AND PHASE CHANGE

21.3.1 Liquid-Vapor Interface

Prediction of surface tension is one of the benchmarks to examine the applicability of the molecular dynamics method and the potential function model to the liquid-vapor interface. Detailed discussions are in the previous review [3]. The typical simulation system is the liquid slab between vapor regions. When the liquid layer is thick enough, the bulk property of liquid can be obtained at the central region, and two liquid-vapor interfaces can be realized. Fig. 21.4 shows an example of such interface calculated with 8000 Lennard-Jones molecules. By taking a time average, the density profile, pressure tensor, and surface tension can be reasonably predicted. Though the normal pressure keeps the constant value, the tangential pressure exhibits a sharp drop near the liquid-vapor interface region. The integrated value of this tangential pressure drop is the surface tension. More, practically, surface tension in the interface can be calculated as

$$\gamma_{\mathrm{LG}} = \int_{z_{\mathrm{L}}}^{z_{\mathrm{G}}} \left[P_{\mathrm{N}}(z) - P_{\mathrm{T}}(z) \right] dz , \quad (21.26)$$

where z is the coordinate perpendicular to the interface and P_{N} and P_{T} are normal and tangential components of pressure. Quite accurate predictions of surface tension have been demonstrated for

Lennard-Jones fluid [75] and water [76] by integrating the difference of normal and tangential components of pressure tensor across the surface.

Another typical benchmark configuration is the liquid droplet surrounded by its vapor [3]. When the size of the droplet is large enough, the bulk property of liquid is expected at the central region. The well-known Young-Laplace equation relates the curvature of a liquid-vapor interface and surface tension to the pressure difference. Thompson et al. [78] used the spherical extension of Irving-Kirkwood's formula to calculate the normal pressure profile. The definition of the radius of a droplet is not straightforward, since the size of the droplet is normally very small and the liquid-vapor interface has a certain width. The equimolar dividing radius is one of the choices but more elaborate discussions based on the statistical mechanics are found in the literature (see references in [3]). Roughly a thousand molecules are enough to calculate the reasonable value of the bulk surface tension for argon. At the other extreme, the surface tension for very small clusters, which may be important in the nucleation theory, should require a completely different approach because such small clusters do not have the well-defined central liquid part assumed in the statistical mechanical discussions.

The determination of the condensation coefficient by molecular dynamics simulations is also a very fascinating task. The condensation coefficient has been simply defined as the ratio of rates of the number of condensation molecules to incident molecules. Through the detailed studies of the liquid-vapor interphase phenomena of argon, water, and methanol, Matsumoto et al. [79, 80] pointed out that this macroscopic concept could not be directly converted to the molecular scale concept and that the ‘molecular exchange’ process must be considered. On the other hand, Tsuruta et al. [81] have reported a significant dependence of the trapping rate on the normal velocity of incident molecules. Recently, Tsuruta et al. [82, 83] successfully modeled the simulated condensation coefficient by a ‘transition state theory’ similar to chemical reaction dynamics.

Molecular dynamics simulations of the effect of surfactant in liquid-vapor interface are also

being developed. An example is the simulation of the effect of n-alcohols in the liquid-vapor interface of water and of LiBr solution by Daiguji [84].

21.3.2 Solid-Liquid-Vapor Interactions

Lennard-Jones Model System

Solid-liquid-vapor interaction phenomena have played a very important role in phase-change heat transfer. The importance of the liquid wetting to the surface is apparent in dropwise condensation, high-heat-flux boiling heat transfer, and capillary liquid-film evaporators. There are good reviews of the connection between microscopic and macroscopic views of the wetting phenomena by Dussan [85], and from a slightly more microscopic point of view by Koplik and Banavar [86]. Furthermore, molecular dynamics treatment of simple Lennard-Jones liquid droplet on the solid surface and Lennard-Jones vapor bubble on the solid surface are discussed in the review [3]. In brief, except for the two or three liquid layers near the surface, the averaged shape of the Lennard-Jones liquid droplet is close to semi-spherical [87-89]. A snapshot of a droplet on the solid surface and the 2D density distribution are compared in Fig. 21.5 [89]. By fitting a circle to the density contour disregarding a few layers of liquid near the solid surface, “contact angle” can be measured. The effect of the interaction potential on the shape of the liquid droplet is summarized in Fig. 21.6 [87-90]. The cosine of measured contact angle is linearly dependent on the strength of the surface potential. The contact angles measured from the droplet and the bubble are almost consistent as several images of 2-D density profiles in the insets of Fig. 21.6. Here, as the measure of the strength of the interaction, the depth of the integrated potential

$$\varepsilon_{SURF} = (4\sqrt{3}\pi/5)(\sigma_{\mathrm{INT}}{}^2 / R_0{}^2)\varepsilon_{\mathrm{INT}} \qquad (21.26)$$

was employed [3]. The controversial discussions whether the Young’s equation can hold or not in such

system has been historically discussed (see references in [3]). However, at least the concept of surface energy balance should be valid. For the macroscopic contact, the well-known Young's equation relates the contact angle to the balance of surface energies as

$$\cos\theta = \frac{\gamma_{SG} - \gamma_{SL}}{\gamma_{LG}} \quad (21.27)$$

where γ_{SG}, γ_{SL} and γ_{LG} are surface energies between solid-gas, solid-liquid, and liquid-gas, respectively. With a change in the energy parameter between liquid and solid molecules, γ_{LG} is kept constant and γ_{SG} does not change much compared with γ_{SL} because the vapor density is much lower compared with liquid density. With increase in ε_{SURF}, γ_{SL} should decrease almost proportionally because of the gain in potential energy in liquid-solid interface. Then, (γ_{SG} - γ_{SL}) should increase and the Young's equation predicts the increase in cosθ. Hence, the linear relation in Fig. 21.6, roughly speaking, is consistent with Young's equation.

Water Droplets on a Platinum Solid Surface

As a more practical simulation of solid-liquid-vapor interaction, a water droplet on a platinum solid surface is shown in Fig. 21.7 [90]. Water molecules were modeled with the SPC/E potential. The interaction potential between water and platinum molecules was expressed by the potential function developed by Zhu and Philpott [91], based on the extended Hückel calculations. The potential function consists of a water-molecule-conduction electron potential, an anisotropic short-range potential, and an isotropic short-range r^{-10} potential as follows.

$$\phi_{\mathrm{H_2O-surf}} = \phi_{\mathrm{H2O-cond}} + \phi_{\mathrm{an}}(\mathrm{O};\mathbf{r}_{\mathrm{O}}) + \phi_{\mathrm{isr}}(\mathrm{O};\mathbf{r}_{\mathrm{O}}) + \sum_{H}\left[\phi_{\mathrm{an}}(\mathrm{H};\mathbf{r}_{\mathrm{H}}) + \phi_{\mathrm{isr}}(\mathrm{H};\mathbf{r}_{\mathrm{H}})\right] \quad (21.28)$$

$$\phi_{\mathrm{H2O-cond}} = \sum_{l,k}\frac{q_l q_k}{2r_{lk}} \quad (21.29)$$

$$\phi_{\mathrm{an}}\left(p;\mathbf{r}_p\right)=4\varepsilon_{p-\mathrm{Pt}}\sum_j\left[\left(\frac{\sigma_{p-\mathrm{Pt}}{}^2}{\left(\alpha\rho_{pj}\right)^2+z_{pj}{}^2}\right)^6-\left(\frac{\sigma_{p-\mathrm{Pt}}{}^2}{\left(\rho_{pj}/\alpha\right)^2+z_{pj}{}^2}\right)^3\right] \qquad (21.30)$$

$$\phi_{\mathrm{isr}}\left(p;\mathbf{r}_p\right)=-4\varepsilon_{p-\mathrm{Pt}}\sum_j\frac{c_{p-\mathrm{Pt}}\sigma_{p-\mathrm{Pt}}{}^{10}}{r_{pj}{}^{10}} \qquad (21.31)$$

where $\alpha = 0.8$, $\sigma_{\mathrm{O\text{-}Pt}} = 0.270$ nm, $\varepsilon_{\mathrm{O\text{-}Pt}} = 6.44\times10^{-21}$ J, $c_{\mathrm{O\text{-}Pt}} = 1.28$, $\sigma_{\mathrm{H\text{-}Pt}} = 0.255$ nm, $\varepsilon_{\mathrm{H\text{-}Pt}} = 3.91\times10^{-21}$ J, $c_{\mathrm{H\text{-}Pt}} = 1.2$. Here, Eq. (21.29) represents Coulomb potential between the point charge of a water molecule and its image charge located at symmetrical position below the image plane. This potential takes the minimum value when a water molecule sits on top of a platinum atom heading hydrogen atoms upward. The contact structure of the water droplet with a finite contact angle on the absorbed monolayer water film in Fig. 21.7 was quite a surprise. It was the first demonstration of such a structure with equilibrium molecular dynamics simulation. Even though the existence of a thin liquid film is sometimes assumed in the liquid-solid contact theories, the simple energy consideration using the Young's equation should conclude that the water droplet should be very wettable to a water film. However, the contact angle is determined by the surface energy between this monolayer water film and bulk liquid water. The monolayer film does not have the characteristics of bulk water. It has quite high density due to the strong interaction to the platinum surface atoms, and the interaction of this film with normal water strongly depends on the density of the film. The higher density of the water monolayer results the lower interaction. With this assumption, the clear dependence of contact angle on the platinum crystal lattice structure can also be explained [91].

21.3.3 Nucleation and Phase Change

Homogeneous Nucleation

Homogeneous nucleation is one of the typical macroscopic phenomena directly affected by

the molecular scale dynamics. Recently, Yasuoka et al. have demonstrated the direct molecular dynamics simulations of the nucleation process for Lennard-Jones fluids [93] and for water [94]. After quenching to the supersaturation condition, the condensation latent heat must be removed for the successive condensation. Yasuoka et al. [93] used 5000 Lennard-Jones molecules for the simulation mixed with 5000 soft-core carrier gas molecules connected to a Nosé-Hoover thermostat for the cooling agent. This cooling method mimicked the carrier gas of supersonic jet experiments. Through the detailed study of growth and delay of nuclei size distribution, they have estimated the nucleation rate and the critical size of nucleus. The nucleation rate was seven orders of magnitude larger than the prediction of classical nucleation theory. Their similar simulation [94] for water of TIP4P potential at 350 K resulted the nucleation rate two orders of magnitude smaller than the classical nucleation theory, just in good agreement with the “pulse expansion chamber” experimental results.

Heterogeneous Nucleation

Heterogeneous nucleation is also important in many heat transfer problems. Fig. 21.8 shows an example of the heterogeneous nucleation of liquid droplet on a solid surface [95]. Argon vapor consisting of 5760 Lennard-Jones molecules was suddenly cooled by the solid wall controlled with the phantom technique [3]. The phantom molecules modeled the infinitely wide bulk solid kept at a constant temperature with proper heat conduction characteristics. The potential between argon and solid molecule was also represented by the Lennard-Jones potential function, and the energy scale parameter was changed to reproduce various wettabilities. After the equilibrium condition at 160 K was obtained, temperature of the solid surface was suddenly set to 100 K or 80 K by the phantom molecule method. Initially, small clusters were appeared and disappeared randomly in space. Then larger clusters grew preferentially near the surface for wettable cases. On the other hand, for the less wettable condition, relatively large clusters grew without the help of surface just like the

homogeneous nucleation. The nucleation rate and free energy needed for cluster formation were not much different from the prediction of the classical heterogeneous nucleation theory in case of lower cooling rates.

A molecular dynamics simulation of homogeneous [96, 97] or heterogeneous [90] nucleation of a vapor bubble is much more difficult compared to the nucleation of a liquid droplet. Even though the formation of a vapor bubble can be reproduced by expanding the liquid to the negative pressure, qualitative comparison of nucleation rate or critical radius is not easy.

21.3.4 Notes on Nucleation and Stability of Nano Bubbles in a Confined System

Direct molecular dynamics simulation of nucleation of bubbles in liquid can be possible and a nanoscale bubble can be stably realized in a confined system. However, the stability of a nanoscale bubble confined in small space is quite different from that in an open space. Here, the stability of a bubble in a confined space is compared with usual classical nucleation theory.

According to the classical nucleation theory, the stability of a vapor bubble depends on the critical radius of the bubble. Appearance of a vapor bubble with radius r in a supersaturated liquid results the reduction of free energy of $\Delta g V_{gas}$ and the increase of surface energy as γA. Hence, the net change in Gibbs free energy is expressed as

$$\Delta G_{\infty} = \gamma A + \Delta g V_{gas} = (4\pi\gamma) r^2 + (\frac{4}{3}\pi\Delta g) r^3, \qquad (21.32)$$

where γ is surface tension, A is surface area = $4\pi r^2$, V_{gas} is volume $\frac{4}{3}\pi r^3$, and Δg is free energy difference between liquid and vapor. The negative value of Δg at supersaturated condition is the driving force of the nucleation of a bubble. Figure 21.9 shows ΔG_{∞} in Eq. (21.32). When r is small, ΔG_{∞} increases with r^2 through the surface energy term. For r larger than the critical value r_{crit}, ΔG_{∞}

decreases with r^3. Hence, a bubble smaller than r_{crit} is unstable and should shrink, but a bubble grown larger than r_{crit} by the statistical fluctuation should stably keep growing.

A nano-bubble confined in a constant small volume, as in the case of usual molecular dynamics simulations, should be controlled by another free energy term in addition to that of Eq. (21.32). The free energy term from the confined liquid should be quite important. The volume occupied by the liquid should decrease with the growth of a vapor bubble, leading to the increase in liquid density. The increase in density of liquid causes a large increase in free energy ΔG_L. Hence, the free energy change in the confined system should contain this ΔG_L term as follows.

$$\Delta G = \Delta G_\infty + \Delta G_L = \gamma A + \Delta g V_{gas} + \Delta g_L V_{liquid} = (4\pi\gamma) r^2 + (\frac{4}{3}\pi\Delta g) r^3 + \Delta g_L (L^3 - \frac{3}{4}\pi r^3) \qquad (21.33)$$

This additional term ΔG_L should be negligible when liquid volume is large enough. Fig. 21.9 shows the expected approximate shape of ΔG_L and $\Delta G = \Delta G_\infty + \Delta G_L$. Here, it is assumed that ΔG_L should gradually decrease with increase in bubble size since the liquid density increases from the negative pressure condition. When the bubble size becomes such that the saturated liquid and vapor co-exist with radius r_{sat}, ΔG_L should become minimum. Further increase in bubble size corresponds to the considerable compression of liquid, hence a rapid increase in ΔG_L is expected. The free energy change can be approximately express by a function of liquid density from

$$\Delta g_L = f(\frac{\rho_L}{\rho_{sat}}) = f\left(\frac{V_{sat}}{V_L}\right) = f\left(\frac{L^3 - \frac{4}{3}\pi r_{sat}^{\ 3}}{L^3 - \frac{4}{3}\pi r^3}\right) \qquad (21.34)$$

The density ratio ρ_L / ρ_{sat} can roughly related to the ratio of intermolecular distance $(\rho_L / \rho_{sat})^{1/3}$. Then, the schematic shape ΔG_L in Fig. 21.9 was drawn by assuming that the free energy should be proportional to the shape of Lennard-Jones potential energy.

It is observed that $\Delta G = \Delta G_\infty + \Delta G_L$ becomes minimum value when the radius is slightly

larger than r_{sat}. Simulated bubbles in a confined system should be stable with this minimum point. When the confined system size is large enough, it is still possible to approximately simulate the nucleation process beyond the critical radius and critical free energy. However, when the system size is smaller or the degree of supersaturation is less, the confinement effect should be much stronger. An example with smaller r_{sat} is shown as $\Delta G_L'$ and $\Delta G_\infty + \Delta G_L'$ in Fig. 21.9. The simulated stable bubble should be much smaller than the critical size for free space and the simulated free energy barrier is much smaller. With further smaller system, $\Delta G_\infty + \Delta G_L'$ should have no minimum value. The same argument is also applicable to a system with a liquid droplet surrounded in its vapor. However, since the change of free energy of vapor with density is not as large as for liquid, a reasonable simulation of the nucleation process is possible with relatively small system.

21.3.5 Crystallization of Amorphous Silicon

An example of a crystal growth process from amorphous silicon is shown in Fig. 21.10 [98]. By using the Tersoff (C) potential [38], the crystallization process was calculated. With the solid phase epitaxy (SPE) configuration [e.g., 99], the crystal growth in (001) and (111) directions were compared. It was observed that growth in (111) direction was dominant in Si crystallization at the high temperature region possibly because of instability of (001) amorphous/crystal (a/c) interface. Then, the newly developed crystallization system that consisted of a Si cluster on an amorphous surface with a small number of seed atoms was also simulated. With this configuration, the artifacts induced by the periodic boundary condition could be completely neglected. From the time profile of the Si crystal nuclei size, the classical critical nuclei size was estimated to be around 110 atoms.

21.3.6 Formation of Clusters, Fullerene, and Carbon Nanotubes

The intermediate cluster structure are extremely important when some of them can be stably observed as the end products such as the simulation of fullerene formations [41, 100] and endohedral metallofullerene formations [101]. The formation mechanism of SWNTs is theoretically interesting and also extremely important for the development of large scale and controlled generation techniques. The molecular dynamics simulation [102] of laser-oven or arc-discharge processes is very much similar to the simulation of endohedral metallofullerene formation, because the actual experimental condition is almost the same except for the small amount of metal doped in the graphite material. Recently, SWNTs formation mechanism for CVD techniques [103-105] is getting more attention because they are expected to supply large amount of SWNTs at a lower cost. In catalyst CVD process, CO [106], hydrocarbon or alcohol [107] will be decomposed on the catalytic metal cluster supported by silica, alumina, magnesia or zeolite. In both process, carbon atoms are supplied to the metal cluster at a high temperature condition.

Figure 21.11 shows the nucleation process of a SWNT in a catalytic CVD process [103]. Using the simplified Brenner [41] potential for carbon-carbon interaction and the empirical metal-carbon potential functions [101], the nucleation process of SWNT by successive collisions of hydrocarbon molecules to a metal cluster was simulated. At first, the initial Ni cluster structures of various sizes were obtained by annealing a fcc crystal at 2 ns in 2000 K. As the initial condition of clustering process, the completely random vapor mixture of 500 carbon atoms and one of the Ni clusters obtained above were allocated in 20 nm cubic fully-periodic simulation cell. The interaction between isolated carbons was represented by the Lennard-Jones potential to avoid the generation of carbon clusters before the collision to the metal catalyst.

In the first stage, all carbon atoms attached to the exposed surface are absorbed in the metal cluster. After saturation within about 2 ns, hexagonal carbon networks are formed inside the metal-carbon binary cluster (Fig. 21.11 (a)). Some of the carbon networks separate from the surface of the particle and in specific cases some cap structures appear, as if the sphere surface of the metal

cluster played as a template for cap formation (Fig. 21.11 (b)). When separation of the carbon network occurs, the area of bare metal surface decreases but some of the open areas are preserved especially in the crystalline part where additional carbon atoms can still flow. Continuous supply of carbon atoms leads to the formation of annular graphitic protrusion (Fig. 21.11 (c)). After the cap coalesces into annular graphitic protrusion (Fig. 21.11 (d)), the larger carbon network covers the surface with a certain curvature (Fig. 21.11 (e)). Furthermore, supersaturated carbon atoms inside the Ni cluster gradually lift up the carbon-shell surface leading to a half-cap structure that appears after 40 ns (Fig. 21.11 (f)). This lifting-up of the carbon cap results in formation of its stem, which can be regarded as an initial stage of the growth process of SWNT (Fig. 21.11 (g, f)).

21.4 HEAT TRANSFER ISSUES OF CARBON NANOTUBES

21.4.1 Introduction of Carbon Nanotubes

Since their discovery by Iijima [108] in 1991, carbon nanotubes shown in Fig. 21.12 have been regarded as one of the most important materials in “nanotechnology.” Due to their novel electronic, optical, and mechanical properties, single-walled carbon nanotubes (SWNTs) [109] show great potential for use in a wide variety of applications [110, 111]. Many applications such as field effect transistors, electron field emission sources, single electron transistors, optical switches, nano-wires, chemical sensors, and composite materials for high mechanical and thermal properties have been examined.

The geometry of an SWNT can be described as a single layer of a graphite sheet that is rolled up into a cylinder. The diameter of the tube varies from 0.7 to about 3 nm and the length is about a few microns to even a few centimeters. The geometry can be specified by the chiral vector

$$\mathbf{C}_h = n\mathbf{a}_1 + m\mathbf{a}_2 \equiv (n, m), \qquad (21.35)$$

where $\boldsymbol{a}_1$ and $\boldsymbol{a}_2$ are unit vectors of the honeycomb lattice of the graphite sheet. By rolling the carbon sheet up so that two atoms at the origin and at $\boldsymbol{C}_h$ in the honeycomb lattice will meet, $\boldsymbol{C}_h$ will be the circumference of the SWNT. Hence, the geometry of a SWNT is uniquely determined by the chiral index (n, m). Details of properties of carbon nanotubes are describes in monographs [110, 111]. The electronic property of SWNT is most exciting that it may be metallic or semiconductor depending on the chirality. The electronic density of states shows divergences called Van Hove singularity. Many of electronic and optical applications are based on these molecular-like DOS structures.

Most of studies of SWNTs have started after the discoveries of macroscopic generation techniques, the laser-furnace method in 1996 and the arc-discharge method in 1997. Recently, the bulk generation of SWNTs by the catalytic CVD process called HiPco [106] was developed. An alternative catalytic CVD method using alcohol as the carbon source was introduced by the author's group [107].

21.4.2 Nanotubes with Fluids

Contact of fluid with a nanotube is an important problem to be solved with molecular dynamics simulations. One example is the hydrogen absorption with SWNTs. Even though absorption of other molecules is quite interesting, the hydrogen case has been the focus of many simulations and experiments because of the technically important problem of hydrogen storage for fuel cell hydrogen source. Contact of water with SWNTs is also quite interesting.

Hydrogen Absorption with Single-Walled Carbon Nanotubes

Since the suggestion of high efficiency storage of hydrogen with SWNTs by Dillon et al. (1997) [112], experimental determinations of the storage capacity and mechanism of storage have

been extensively studied. Hydrogen storage capacity of high purity SWNT was reported to be more than 8 wt % at 12 MPa and 80 K [113], or 4.2 wt % at 10 MPa at room temperature [114]. Recent experimental studies are concluding that the hydrogen storage capacity of SWNTs at room temperature is less than 1 wt % [115]. Most of molecular dynamics simulations have been consistently predicting the very low hydrogen storage capacity at room temperature [116, 117].

An example of molecular dynamics simulation of hydrogen absorption is shown in Fig. 21.13 [118]. Assuming the physical adsorption of hydrogen to the surface of carbon nanotubes, potential forms between H_2-H_2 and C-H_2 were both expressed by Lennard-Jones (12-6) functions, with parameters: ε_{HH} = 3.180 meV, σ_{HH} = 2.928 Å, ε_{HC} = 2.762 meV and σ_{HC} = 3.179 Å. Each nanotube was regarded as rigid molecule and the van der Waals potential between nanotubes was derived as a Lennard-Jones (8-4) function by integrating the potential function between carbon atoms. The potential energy has minimum at the interstitial sites (between nanotube), and has a low value at the endohedral sites (inside a nanotube). The interaction potential is too weak for the efficient hydrogen storage at room temperature for the use in fuel-cell vehicles.

Water in Carbon Nanotubes

Some recent experimental works [119, 120] shows the trapped aqueous solution in MWNTs generated with a hydrothermal method. Even though the contents of this aqueous solution are unclear, the liquid- and vapor- interface structure and phase-change in the completely closed space of about 50 nm are truly exciting. The solution was quite wetting to the walls of carbon nanotubes. Another experimental work [121] suggests that liquids with a surface tension lower than 100-200 mNm^{-1} can wet a carbon nanotube. Therefore, it is expected that water, with a surface tension of 73 mNm^{-1}, should wet carbon nanotube. Figure 21.14 shows a snapshot of a water cluster in a SWNT with quite a large diameter of 2.77 nm. The interaction potential between carbon and water is simply

Lennard-Jones function between carbon and oxygen atom. The interaction parameters are ε_{OC} = 1.08×10^{-21} J and σ_{OC} = 0.316 nm. It is clearly seen that the water cluster is not very wetting but the potential energy is lower than in vacuum. Walther et al. [122, 123] studied the wetting phenomena of SWNTs more in detail by molecular dynamics simulations. In addition to the Lennard-Jones potential between oxygen and carbon, a quadrupole interaction between the carbon and the partial charges on hydrogen and oxygen atoms was also considered. The simulation results show that pure water does not wet a carbon nanotube. Just like graphite, the wall of nanotube is strongly hydrophobic.

Koga et al. [124] found an ice-nanotube structure in an SWNT by molecular dynamics simulations. Maniwa et al. [125] showed consistent experimental results later.

21.4.3 Heat Conduction of Carbon Nanotubes

A heat conduction simulation along a carbon nanotube is shown in Fig. 21.15 [126, 127]. The thermal conductivity of nanotubes, which was speculated to be higher than any other material along the cylindrical axis [128] was measured from the simulations for nanotubes with several different chiralities and lengths. The potential function employed was the simplified Brenner bond order potential [41]. The temperature at each end of a nanotube was controlled by the phantom technique [3], and no periodic boundary condition was applied in order to simulate the finite length effect. The thermal conductivity was calculated from the measured temperature gradient as in Fig. 21.16 and the heat flux obtained by the integration of the additional force by the phantom molecules. The preliminary result showed that the thermal conductivity was about 200 ~ 600 W/mK but was strongly dependent on the nanotube length. The power-law behavior of thermal conductivity suggests the divergence for infinitely long system as discussed by Lepri et al. [129, 130].

As the first step to connect the molecular dynamics simulation to the phonon concept approach, phonon density of states and phonon dispersion relations were extracted from the simulated

trajectories. The phonon density of states was measured as the power spectra of velocity fluctuations in Eq. (21.36).

$$D_\alpha(\omega) = \int dt \exp(-i\omega t)\langle v_\alpha(t) v_\alpha(0)\rangle \qquad (21.36)$$

Here, α takes r, θ, z for each velocity component in the cylindrical coordinate. The calculated density of states is shown in Fig. 21.17 as the right hand side inserts of phonon dispersion relations. For this calculation, 8192 temporal data points saved every 5 fs were used.

The photon dispersion relations were also directly measured as the time-space 2-D Fourier transforms in Eq. (21.38) of the displacement vector $r'(z, t)$ from the equilibrium position $r_e(z)$;

$$\mathbf{r}'(z,t) = \mathbf{r}(z,t) - \mathbf{r}_e(z)\,. \qquad (21.37)$$

$$R_\alpha'(k,\omega) = \int dt\, r_\alpha'(z,t)\exp(ikz - i\omega t) \qquad (21.38)$$

Here, k is the wave vector along z-axis. Position vectors $r(z, t)$ of atoms in a line along the z-direction separated by $a = \sqrt{3}a_{c-c}$ ($a_{c\text{-}c}$: bond length) are used. In the case of Fig. 21.17, 128 data points in the z direction multiplied by 8192 temporal points were used. The phonon dispersion relation obtained from eigenvalues and eigenvectors of the dynamical matrix were made with the force-constant tensor scaled from 2 D graphite [131] as shown in Fig. 21.17(d) as the comparison.

21.4.4 Thermal Boundary Resistance between a Carbon Nanotube and Surrounding Materials

In addition to the thermal conductivity along an SWNT, heat transfer from a nanotube to the surrounding material is an important issue for practical applications using carbon nanotubes as electrical devices and composite materials. The heat transfer rate can be well expressed by the thermal boundary resistance, or the thermal conductance through the boundary. The thermal conductance of a nanotube junction, the heat transfer from an SWNT to other SWNTs, and the heat transfer from an SWNT to water are introduced here for examples [132]. In this chapter, interfacial thermal

conductance K is used. The thermal boundary resistance R_T is simply calculated as $R_T = 1/K$, where K is the thermal conductance.

Thermal Conductance at an SWNT Junction

A junction of nanotubes with different chiralities is shown in Fig. 21.18. In this case a (12, 0) zigzag nanotube in the left-hand side and a (6, 6) armchair nanotube were smoothly connected using 5-membered and 7-membered rings at the junction. By applying different temperatures at each end, the temperature distribution was measured as in the bottom panel of Fig. 21.18. The temperature jump at the junction is clearly observed. This temperature jump can be modeled by assuming that there is a virtual boundary between two nanotubes with different structures. The thermal conductance at the virtual interface is defined as the heat transfer through the boundary, hence,

$$K \equiv h = \frac{Q}{A\Delta T}. \qquad (21.39)$$

The thermal conductance at the junction is calculated as 1.4×10^4 MW/m^{2}K. Here, the cross-sectional area was defined as πbd [132].

Thermal Boundary Resistance of SWNT Bundles

As the initial condition, a bundle of 7 SWNTs arrange as in Fig. 21.12 (b) with the length of 5 nm were placed in a 5×6×6 nm simulation cell. The geometrical structure of the SWNT was the armchair type (5, 5) with 0.693 nm diameter. At the beginning of the computation, the whole system was kept at 300 K for 100 ps. Then, the temperature of the central SWNT was suddenly increased to 400 K using the velocity scaling method for 10 ps. After that, all the temperature controls were turned off. Fig. 21.19(a) shows a time history of the temperature of the hot (central) tube and cold (surrounding) tubes. Here, the heat transfer from the central tube to surrounding tubes is clearly

observed. In order to examine this heat transfer, temperature differences between the central and surrounding tubes are drawn in Fig. 21.19(b). The monotonic decay of the temperature difference in Fig. 21.19(b) was well approximated by an exponential function;

$$T_{hot} - T_{cold} = T_0 \exp\left(-\frac{t}{\tau}\right), \qquad (21.40)$$

where T_0 = 875 [K] and τ = 29.7 [ps].

If an SWNT is considered to be a solid material and heat transfer from the central tube to surrounding tubes is expressed by heat transfer coefficient or thermal conductance at the boundary, the lumped capacity method in Eq. (21.41) can be adopted since the characteristic length of an SWNT is extremely small. The diameter of SWNT is about 1 nm and the Biot number in Eq. (21.42) becomes extremely small.

$$T_{hot} - T_{cold} = T_0 \exp\left[-\left(\frac{1}{\rho_{hot} c_{hot} V_{hot}} + \frac{1}{\rho_{cold} c_{cold} V_{cold}}\right) KSt\right]. \qquad (21.41)$$

$$Bi = \frac{hL}{\lambda} \quad (21.42)$$

The excellent agreement to an exponential fit by Eq. (21.40) in Fig. 21.19 is understood by the concept mentioned above. Comparing Eq. (21.40) with Eq. (21.41), the thermal conductance K was estimated. The thermal conductance between SWNTs in a bundle [132] was calculated to be about 15 MW/m^{2}K.

Thermal Boundary Resistance between an SWNT and Water

One (10, 10) SWNT with length 20.118 nm containing 192 water molecules were prepared in the 20.118×10×10 nm fully-periodic simulation cell in the similar configuration as in Fig. 21.14. At the initial stage of simulation, water molecules and the SWNT were equilibrated at temperature of 300 K. Then, only the temperature of the SWNT was suddenly heated up to 400K. After applying the heat

for 1 ps, all temperature control was turned off. The interfacial thermal conductance is calculated to be 8 MW/m^{2}K using the lumped capacity method similarly to the case of SWNT bundle simulation [132].

Very recently, Huxtable et al. [133] reported nanotube-SDS interfacial thermal conductance as K = 12 MW/m^{2}K by picosecond transient absorption experiments. Shenogin et al. [134] obtained K = 20 MW/m^{2}K for octane-nanotube interface by their molecular dynamics simulations for long enough nanotubes. Furthermore, physical mechanism of thermal conductance is being explored through molecular dynamics simulations [135].

References

[1] M. P. Allen and D. J. Tildesley, *Computer Simulation of Liquids*, Oxford University Press, New York, 1987.

[2] J. M. Haile, *Molecular Dynamics Simulation*, John Wiley & Sons, New York, 1992.

[3] S. Maruyama, Molecular Dynamics Method for Microscale Heat Transfer, *Advances in Numerical Heat Transfer*, vol. 2, ed. W. J. Minkowycz and E. M. Sparrow, Taylor & Francis, Washington D. C., pp. 189-226, 2000.

[4] S. Maruyama, Molecular Dynamics Methods in Microscale Heat Transfer, *Handbook of Heat Exchanger Update*, Begell House, New York, pp. 2.13.7-1-2.13.7-33, 2002.

[5] T. Ohara, Molecular Dynamics Study in Microscale Thermophysical Engineering: Current Activities and Future in Japan, *Micro. Thermophys. Eng.*, vol. 4, no. 4, pp. 213-221, 2000.

[6] D. Poulikakos, S. Arcidiacono and S. Maruyama, Molecular Dynamics Simulations in Nanoscale Heat Transfer: A Review, *Micro. Thermophys. Eng.*, vol. 7, no. 3, pp. 181-206, 2003.

[7] A. Majumdar, Nanoengineering: Promises and Challenges, *Micro. Thermophys. Eng.*, vol. 4, no. 2, pp. 77-82, 2000.

[8] D. G. Cahill, W. K. Ford, K. E. Goodson, G. D. Mahan, A. Majumdar, H. J. Maris, R. Merlin and S. R. Phillpot, Nanoscale Thermal Transport, *J. Appl. Phys.*, vol. 93, no. 2, pp. 793-818, 2003.

[9] J. O. Hirschfelder, C. F. Curtiss and R. B. Bird, *Molecular Theory of Gases and Liquids*, John Wiley & Sons, New York, 1954.

[10] G. A. Bird, *Molecular Gas Dynamics and the Direct Simulation of Gas Flow*, Oxford University Press, New York, 1994.

[11] C. Kittel, *Introduction to Solid State Physics*, 7th ed., John Wiley & Sons, New York, 1996.

[12] G. Chen, Thermal Conductivity and Ballistic-Phonon Transport in the Cross-Plane Direction of Superlattices, *Phys. Rev. B*, vol. 57, no. 23, pp. 14958-14973, 1998.

[13] A. J. H. McGaughey and M. Kaviany, Quantitative Validation of the Boltzmann Transport

Equation Phonon Thermal Conductivity Model Under the Single-mode Relaxation Time Approximation, *Phys. Rev. B*, vol. 69, pp. 094303-1-094303-12, 2004.

[14] N. Mingo, L. Yang, D. Li, and A. Majumdar, Predicting the Thermal Conductivity of Si and Ge Nanowires, *Nanoletters*, vol. 3, no. 12, pp. 1713-1716, 2003.

[15] J. J. Nicolas , K. E. Gubbins, W. B. Streett and D. J. Tildesley, Equation of State for the Lennard-Jones Fluid, *Molecular Physics*, vol. 37-5, pp. 1429-1454, 1979.

[16] F. H. Lee, Analytic Representation of Thermodynamics Data for the Lennard-Jones Fluid, *J. Chem. Phys.*, vol. 73, no. 10, pp. 5401-5403, 1980.

[17] J. P. Hansen and L. Verlet, Phase Transitions of the Lennard-Jones System, *Phys. Rev.*, vol. 184, pp. 151-161, 1969.

[18] S. D. Stoddard and J. Ford, Numerical Experiments on the Stochastic Behavior of a Lennard-Jones Gas System, *Phys. Rev. A*, vol. 8, pp. 1504-1512, 1973.

[19] M. J. P. Nijmeijer, A. F. Bakker, C. Bruin and J. H. Sikkenk, A Molecular Dynamics Simulation of the Lennard-Jones Liquid-Vapor Interface, *J. Chem. Phys.*, vol. 89, no. 6, pp. 3789-3792, 1988.

[20] H. J. C. Berendsen, J. P. M. Postma, W. F. van Gunsteren and J. Hermans, in *Intermolecular Forces* (ed. B. Pullmann), Reidel, Dordrecht, p. 331, 1981.

[21] H. J. C. Berendsen, J. R. Grigera and T. P. Straatsma, The Missing Term in Effective Pair Potentials, *J. Phys. Chem.*, vol. 91, no. 24, pp.6269-6271, 1987.

[22] W. L. Jorgensen, J. Chandrasekhar, J. D. Madura, R. W. Impey and M. L. Klein, Comparison of Simple Potential Functions for Simulating Liquid Water, *J. Chem. Phys.*, vol. 79, no. 2, pp. 926-935, 1983.

[23] W. L. Jorgensen, Optimized Intermolecular Potential Functions for Liquid Alcohols, *J. Phys. Chem.*, vol. 90, pp. 1276-1284, 1986.

[24] V. Carravetta and E. Clementi, Water-Water Interaction Potential: An Approximation of the

Electron Correlation Contribution by a Function of the SCF Density Matrix, *J. Chem. Phys.*, vol. 81, no. 6, pp. 2646-2651, 1984.

[25] J. Alejandre, D. J. Tildesley and G. A. Chapela, Molecular Dynamics Simulation of the Orthobaric Densities and Surface Tension of Water, *J. Chem. Phys.*, vol. 102, no. 11, pp. 4574-4583, 1995.

[26] L. X. Dang and T-M. Chang, Molecular Dynamics Study of Water Clusters, Liquid, and Liquid-Vapor Interface of Water with Many-Body Potentials, *J. Chem. Phys.*, vol. 106, no. 19, pp. 8149-8159, 1997.

[27] C. P. Lawrence and J. L. Skinner, Flexible TIP4P Model for Molecular Dynamics Simulation of Liquid Water, *Chem. Phys. Lett.*, vol. 372, pp. 842-847, 2003.

[28] U. Niesar, G. Corongiu, E. Clementi, G. R. Kneller and D. K. Bhattacharya, Molecular Dynamics Simulations of Liquid Water Using the NCC ab initio Potential, *J. Phys. Chem.*, vol. 94, no. 20, pp. 7949-7956, 1990.

[29] D. N. Bernardo, Y. Ding, K. K-Jespersen and R. M. Levy, An Anisotropic Polarizable Water Model: Incorporation of All-Atom Polarizabilities into Molecular Mechanics Force Fields, *J. Phys. Chem.*, vol. 98, pp. 4180-4187, 1994.

[30] W. L. Jorgensen, J. D. Madura and C. J. Swenson, Optimized Intermolecular Potential Functions for Liquid Hydrocarbons, *J. Am. Chem. Soc.*, 106, 6638 (1984).

[31] J. P. Hansen and I. R. McDonald, *Theory of Simple Liquids*, 2nd ed. Academic Press, London, 1986.

[32] S. J. Weiner, P. A. Kollman, D. A. Case, U. C. Singh, C. Ghio, G. Alagona, S. Profeta, Jr. and P. Weiner, A New Force Field for Molecular Mechanical Simulation of Nucleic Acids and Proteins, *J. Am. Chem. Soc.*, vol. 106, pp. 765-784, 1984.

[33] W. D. Cornell, P. Cieplak, C. I. Bayly, I. R. Gould, K. M. Merz, Jr., D. M. Ferguson, D. C. Spellmeyer, T. Fox, J. W. Caldwell and P. A. Kollman, A Second Generation Force Field for the

Simulation of Proteins, Nucleic Acids, and Organic Molecules, *J. Am. Chem. Soc.*, vol. 117, pp. 5179-5197, 1995.

[34] P. Cieplak, J. Caldwell and P. Kollman, Molecular Mechanical Models for Organic and Biological Systems Going Beyond the Atom Centered Two Body Additive Approximation: Aqueous Solution Free Energies of Methanol and N-Methyl Acetamide, Nucleic Acid Base, and Amide Hydrogen Bonding and Chloroform/Water Partition Coefficients of the Nucleic Acid Bases, *J. Computat. Chem.*, vol. 22, pp. 1048-1057, 2001.

[35] D.A. Case, D.A. Pearlman, J.W. Caldwell, T.E. Cheatham III, J. Wang, W.S. Ross, C.L. Simmerling, T.A. Darden, K.M. Merz, R.V. Stanton, A.L. Cheng, J.J. Vincent, M. Crowley, V. Tsui, H. Gohlke, R.J. Radmer, Y. Duan, J. Pitera, I. Massova, G.L. Seibel, U.C. Singh, P.K. Weiner and P.A. Kollman (2002), *AMBER 7*, University of California, San Francisco.

[36] F. H. Stillinger and T. A. Weber, Computer Simulation of Local Order in Condensed Phase of Silicon, *Phys. Rev. B*, vol. 31, no. 8, pp. 5262-5271, 1985.

[37] J. Tersoff, New Empirical Approach for the Structure and Energy of Covalent Systems, *Phys. Rev. B*, vol. 37, no. 12, pp. 6991-7000, 1988.

[38] J. Tersoff, Empirical Interatomic Potential for Silicon with Improved Elastic Properties, *Phys. Rev. B*, vol. 38, no. 14, pp. 9902-9905, 1988.

[39] J. Tersoff, Modeling Solid-State Chemistry: Interatomic Potentials for Multicomponent Systems, *Phys. Rev. B*, vol. 39, no. 8, pp. 5566-5568, 1989.

[40] D. W. Brenner, Empirical Potential for Hydrocarbons for Use in Simulating the Chemical Vapor Deposition of Diamond Films, *Phys. Rev. B*, vol. 42, pp.9458-9471, 1990.

[41] Y. Yamaguchi and S. Maruyama, A Molecular Dynamics Simulation of the Fullerene Formation Process, *Chem. Phys. Lett.*, vol. 286, no. 3-4, pp. 336-342, 1998.

[42] D. W. Brenner, O. A. Shenderova, J. A. Harrison, S. J. Stuart, B. Ni and S. B. Sinnott, A Second-Generation Reactive Empirical Bond Order (REBO) Potential Energy Expression for

Hydrocarbons, *J. Phys.: Condens. Matter*, vol. 14, pp. 783-802, 2002.

[43] L. A. Girifalco and V. G. Weizer, Application of the Morse Potential Function to Cubic Metals, *Phys. Rev.*, vol. 114, pp. 687-690, 1959.

[44] R. A. Johnson, Empirical Potentials and Their Use in the Calculation of Energies of Point Defects in Metals, *J. Phys. F: Metal Phys.*, vol. 3, pp. 295-321, 1973.

[45] M. S. Daw and M. I. Baskes, Semiempirical, Quantum Mechanical Calculation of Hydrogen Embrittlement in Metals, *Phys. Rev. Lett.*, vol. 50, pp. 1285-1288, 1983.

[46] M. S. Daw and M. I. Baskes, Embedded-Atom Method: Derivation and Application to Impurities, Surfaces, and Other Defects in Metals, *Phys. Rev. B*, vol. 29, pp. 6443-6453, 1984.

[47] S. M. Foiles, M. I. Baskes, and M. S. Daw, Embedded-Atom-Method Functions for the fcc Metals Cu, Ag, Au, Ni, Pd, Pt, and Their Alloys, *Phys. Rev. B*, vol. 33, pp. 7983-7991, 1986.

[48] M. I. Baskes, Application of the Embedded-Atom Method to Covalent Materials: A Semiempirical Potential for Silicon, *Phys. Rev. Lett.*, vol. 59, pp. 2666-2669, 1987.

[49] M. I. Baskes, J. S. Nelson and A. F. Wright, Semiempirical Modified Embedded-Atom Potentials for Silicon and Germanium, *Phys. Rev. B*, vol. 40, pp. 6085-6100, 1989.

[50] M. I. Baskes, Modified Embedded-Atom Potentials for Cubic Materials and Impurities, *Phys. Rev. B*, vol. 46, pp. 2727-2742, 1992.

[51] M. I. Baskes and R. A. Johnson, Modified Embedded Atom Potentials for HCP Metals, *Modelling Simul. Mater. Sci. Eng.*, vol. 2, pp. 147-163, 1994.

[52] M. I. Baskes, J. E. Angelo and C. L. Bisson, Atomistic Calculations of Composite Interfaces, *Modelling Simul. Mater. Sci. Eng.*, vol. 2, pp. 505-518, 1994.

[53] H. C. Anderson, Molecular Dynamics Simulations at Constant Pressure and/or Temperature, *J. Chem. Phys.*, vol. 72, no. 4, pp. 2384-2393, 1980.

[54] S. Nosé, A Unified Formulation of the Constant Temperature Molecular Dynamics Methods, *J. Chem. Phys.*, vol. 81, no. 1, pp. 511-519, 1984.

[55] W. G. Hoover, Canonical Dynamics: Equilibrium Phase-Space Distributions, *Phys. Rev. A*, vol. 31, no. 3, pp. 1695-1697, 1985.

[56] M. Parrinello and A. Rahman, Crystal Structure and Pair Potentials: a Molecular Dynamics Study, *Phys. Rev. Lett.*, vol. 45, pp. 1196-1199, 1980.

[57] M. Parrinello and A. Rahman, Polymorphic Transitions in Single Crystal: a New Molecular Dynamics Method, *J. Appl. Phys.*, vol. 52, pp. 7182-7190, 1981.

[58] H. J. C. Berendsen, J. P. M. Postma, W. F. van Gunsteren, A. DiNola, and J. R. Haak, Molecular Dynamics with Coupling to an External Bath, *J. Chem. Phys.*, vol. 81, no. 8, pp. 3684-3690, 1984.

[59] D. J. Evans, Homogeneous NEMD Algorithm for Thermal Conductivity: Application of Non-Canonical Linear Response Theory, *Phys. Lett.*, vol. 91A, pp. 457-460, 1982.

[60] D. J. Evans and G. P. Morriss, *Statistical Mechanics of Non Equilibrium Liquids*, Academic Press, London 1990.

[61] R. Vogelsang, C. Hoheisel and G. Ciccotti, Thermal Conductivity of the Lennard-Jones Liquid by Molecular Dynamics Calculations, *J. Chem. Phys.*, vol. 86, pp. 6371-6375, 1987.

[62] P. K. Schelling, S. R. Phillpot and P. Keblinski, Comparison of Atomic-Level Simulation Methods for Computing Thermal Conductivity, *Phys. Rev. B*, vol. 65, pp. 144306/1-144306/12, 2002.

[63] T. Ohara, Intermolecular Energy Transfer in Liquid Water and Its Contribution to Heat Conduction: An Molecular Dynamics Study, *J. Chem. Phys.*, vol. 111, pp. 6492-6500, 1999.

[64] T. Ohara, Contribution of Intermolecular Energy Transfer to Heat Conduction in a Simple Liquid, *J. Chem. Phys.*, vol. 111, pp. 9667-9672, 1999.

[65] C. L. Tien, J. R. Lukes and F.-C.Chou, Molecular Dynamics Simulation of Thermal Transport in Solids, *Micro. Thermophys. Eng.*, vol. 2, pp. 133-137, 1998.

[66] M. Matsumoto, M. Komiyama, T. Makino and H. Wakabayashi, MD Simulation and Phonon Analysis for Heat Conduction in Solids, *Proc. 37th Japan Heat Transfer Conf.*, vol. 3, pp.

975-976, 2000.

[67] S.-H. Choi and S. Maruyama, Variations in the Thermal Conductivity of Insulating Thin Films with Temperature and Pressure, *J. Kor. Phys. Soc.*, vol. 45, no. 4, pp. 897-906, 2004.

[68] S.-H. Choi, S. Maruyama, K.-K Kim and J.-H. Lee, Evaluation of the Phonon Mean Free Path in Thin Films by using Classical Molecular Dynamics, *J. Kor. Phys. Soc.*, vol. 43, no. 5, pp. 747-753, 2003.

[69] S. Volz, R. Carminati and K. Joulain, Thermal Response of Silicon Crystal to Pico-Femtosecond Heat Pulse by Molecular Dynamics, *Micro. Thermophys. Eng.*, vol. 8, no. 2, pp. 155-167, 2004.

[70] S. Maruyama and T. Kimura, A Study on Thermal Resistance over a Solid-Liquid Interface by the Molecular Dynamics Method, *Thermal Sci. Eng.*, vol. 7, no. 1, pp. 63-68, 1999.

[71] T. Ohara and D. Suzuki, Intermolecular Energy Transfer at a Solid-Liquid Interface, *Micro. Thermophys. Eng.*, vol. 4, no. 3, pp. 189-196, 2000.

[72] L. Xue, P. Keblinski, S. R. Phillpot, S. U. S. Choi and J. A. Eastman, Two Regimes of Thermal Resistance at a Liquid-Solid Interface, *J. Chem. Phys.*, vol. 118, no.1, 2003.

[73] B. C. Daly and H. J. Maris, Calculation of the Thermal Conductivity of Superlattices by Molecular Dynamics Simulation, *Physica B*, vol. 316-317, pp. 247-249, 2002.

[74] M. Matsumoto, H. Wakabayashi and T. Makino, Thermal Resistance of Crystal Interface: Molecular Dynamics Simulation, *Trans. JSME, Ser. B*, vol. 68, no. 671, pp. 1919-1925, 2002.

[75] S.-H. Choi, S. Maruyama, K.-K Kim and J.-H. Lee, Feasibility Study of a New Model for the Thermal Boundary Resistance at Thin Film Interfaces, *J. Kor. Phys. Soc.*, vol. 44, no. 2, pp. 317-325, 2004.

[76] M. J. P. Nijmeijer, A. F. Bakker, C. Bruin and J. H. Sikkenk, A Molecular Dynamics Simulation of the Lennard-Jones Liquid-Vapor Interface, *J. Chem. Phys.*, vol. 89, no. 6, pp. 3789-3792, 1988.

[77] J. Alejandre, D. J. Tildesley and G. A.Chapela, Molecular Dynamics Simulation of the Orthobaric Densities and Surface Tension of Water, *J. Chem. Phys.*, vol. 102, no. 11, pp. 4574-4583, 1995.

[78] S. M. Thompson, K. E. Gubbins, J. P. R. B. Walton, R. A. R. Chantry and J. S. Rowlinson, A Molecular Dynamics Study of Liquid Drops, *J. Chem. Phys.*, vol. 81, no. 1, pp. 530-542,1984.

[79] K. Yasuoka, M. Matsumoto and Y. Kataoka, Evaporation and Condensation at a Liquid Surface. I. Argon, *J. Chem. Phys.*, vol. 101, no. 9, pp. 7904-7911, 1994.

[80] M. Matsumoto, K. Yasuoka and Y. Kataoka, Evaporation and Condensation at a Liquid Surface. II. Methanol, *J. Chem. Phys.*, vol. 101, no. 9, pp. 7911-7917, 1994.

[81] T. Tsuruta, H. Tanaka, K. Tamashima and T. Masuoka, Condensation Coefficient and Interphase Mass Transfer, *International Symposium on Molecular and Microscale Heat Transfer in Materials Processing and Other Applications* (ed. I. Tanasawa and S. Nishio), Begell House, New York, International Center Heat Mass Transfer Symposium, Yokohama, pp. 229-240, 1997.

[82] G. Nagayama and T. Tsuruta, A Generalized Expression for the Condensation Coefficient Based on Transition State Theory and Molecular Dynamics Simulation, *J. Chem. Phys.*, vol. 118, no. 3, pp. 1392-1399, 2003.

[83] T. Tsuruta and G. Nagayama, Molecular Dynamics Studies on the Condensation Coefficient of Water, *J. Phys. Chem. B*, vol. 108, pp. 1736-1743, 2004.

[84] H. Daiguji, Molecular Dynamics Study of n-Alcohols Adsorbed on an Aqueous Electrolyte Solution, *J. Chem. Phys.*, vol. 115, no. 4, pp. 1538-1549, 2001.

[85] V. E. B. Dussan, On the Spreading of Liquids on Solid Surfaces: Static and Dynamic Contact Lines, *Ann. Rev. Fluid Mech.*, vol. 11, pp. 371-400, 1979.

[86] J. Koplik and J. R. Banavar, Continuum Deductions from Molecular Hydrodynamics, *Ann. Rev. Fluid Mech.*, vol. 27, pp. 257-292, 1995.

[87] S. Matsumoto, S. Maruyama and H. Saruwatari, A Molecular Dynamics Simulation of a

Liquid Droplet on a Solid Surface, *Proc. ASME-JSME Thermal Eng. Joint Conf.*, Maui, U.S.A., March 19-24, 1995, Vol. 2, pp. 557-562, 1995.

[88] S. Maruyama, T. Kurashige, S. Matsumoto, Y. Yamaguchi and T. Kimura, Liquid Droplet in Contact with a Solid Surface, *Micro. Thermophys. Eng.*, vol. 2, no.1, pp. 49-62, 1998.

[89] S. Maruyama, T. Kimura and M.-C. Lu, Molecular Scale Aspects of Liquid Contact on a Solid Surface, *Therm. Sci. Eng.*, vol. 10, no.6, pp. 23-29, 2002.

[90] S. Maruyama and T. Kimura, A Molecular Dynamics Simulation of a Bubble Nucleation on Solid Surface, *Int. J. Heat & Technology*, vol. 8, no. 1, pp. 69-74, 2000.

[91] T. Kimura and S. Maruyama, Molecular Dynamics Simulation of Water Droplet in Contact with Platinum Surface, *Proc. 12th Int. Heat Transfer Conf.*, Grenoble, pp. 537-542, 2002.

[92] S.-B.Zhu and M. R. Philpott, Interaction of Water with Metal Surfaces, *J. Chem. Phys.*, vol. 100, no. 9, pp. 6961-6968, 1994.

[93] K.Yasuoka and M. Matsumoto, Molecular Dynamics of Homogeneous Nucleation in the Vapor Phase. I. Lennard-Jones Fluid, *J. Chem. Phys.*, vol. 109, no. 19, pp. 8451-8462, 1998.

[94] K. Yasuoka and M. Matsumoto, Molecular Dynamics of Homogeneous Nucleation in the Vapor Phase. II. Water, *J. Chem. Phys.*, vol. 109, no. 19, pp. 8463-8470, 1998.

[95] T. Kimura and S. Maruyama, A Molecular Dynamics Simulation of Heterogeneous Nucleation of a Liquid Droplet on Solid Surface, *Micro. Thermophys. Eng.*, vol. 6, no. 1, pp. 3-13, 2002.

[96] T. Kinjo and M. Matsumoto, Cavitation Processes and Negative Pressure, *Fluid Phase Equilibria*, vol. 144, pp. 343-350, 1998.

[97] Y. W. Wu and C. Pan, A Molecular Dynamics Simulation of Bubble Nucleation in Homogeneous Liquid under Heating with Constant Mean Negative Pressure, *Micro. Thermophys. Eng.*, vol. 7, pp. 137-151, 2003.

[98] S. Maruyama and T. Inoue, MD Simulation of Crystallization Process of Silicon, *Proc. 38th*

Japan Heat Transfer Conf., pp. 343-344, 2001.

[99] G. H. Gilmer, H. Huang and C. Roland, Thin Film Deposition: Fundamentals and Modeling, *Comp. Mat. Sci.*, vol. 12, pp. 354-380, 1998.

[100] S. Maruyama and Y. Yamaguchi, A Molecular Dynamics Demonstration of Annealing to a Perfect C_{60} Structure, *Chem. Phys. Lett.*, vol. 286, no. 3,4, pp. 343-349, 1998.

[101] Y. Yamaguchi and S. Maruyama, A Molecular Dynamics Study on the Formation of Metallofullerene, *Euro. Phys. J. D*, vol. 9, no. 1-4, pp. 385-388, 1999.

[102] Y. Shibuta and S. Maruyama, Molecular Dynamics Simulation of Generation Process of SWNTs, *Physica B*, 323-1-4, 187-189, 2002.

[103] Y. Shibuta and S. Maruyama, Molecular Dynamics Simulation of Formation Process of Single-Walled Carbon Nanotubes by CCVD Method, *Chem. Phys. Lett.*, vol. 382, no. 3-4, pp. 381-386, 2003.

[104] F. Ding, A. Rosen and K. Bolton, The Role of the Catalytic Particle Temperature Gradient for SWNT Growth from Small Particles, *Chem. Phys. Lett.*, vol. 393, pp. 309-313, 2004.

[105] F. Ding, K. Bolton and A. Rosen, Nucleation and Growth of Single-Walled Carbon Nanotubes: A Molecular Dynamics Study, *J. Phys. Chem. B*, vol. 108, pp. 17369-17377, 2004.

[106] M. J. Bronikowski, P. A. Willis, D. T. Colbert, K. A. Smith and R. E. Smalley, Gas-Phase Production of Carbon Single-Walled Nanotubes from Carbon Monoxide via the HiPco Process: A Parametric Study, *J. Vac. Sci. Technol. A*, vol. 19, pp. 1800-1805, 2001.

[107] S. Maruyama, R. Kojima, Y. Miyauchi, S. Chiashi and M. Kohno, Low-Temperature Synthesis of High-Purity Single-Walled Carbon Nanotubes from Alcohol, *Chem. Phys. Lett.*, vol. 360, no. 3-4, pp. 229-234, 2002.

[108] S. Iijima, Helical Microtubules of Graphitic Carbon, *Nature*, vol. 354, pp. 56-58, 1991.

[109] S. Iijima and T. Ichihashi, Single-Shell Carbon Nanotubes of 1-nm Diameter, *Nature*, vol. 363, pp. 603-605, 1993.

[110] M. S. Dresselhaus and G. Dresselhaus, *Science of Fullerenes and Carbon Nanotubes*, Academic Press, New York, 1996.

[111] R. Saito, G. Dresselhaus and M. S. Dresselhaus, *Physical Properties of Carbon Nanotubes*, Imperial College Press, London, 1998.

[112] A. C. Dillon, K. M. Jones, T. A. Bekkedahl, C. H. Kiang, D. S. Bethune and M. J. Heben, Storage of Hydrogen in Single-Walled Carbon Nanotubes, *Nature*, vol. 386, no. 27, pp. 377-379, 1997.

[113] Y. Ye, C. C. Ahn, C. Witham, B. Fultz, J. Liu, A. G. Rinzler, D. Colbert, K. A. Smith and R. E. Smalley, Hydrogen Adsorption and Cohesive Energy of Single-Walled Carbon Nanotubes, *Appl. Phys. Lett.*, vol. 74, no. 16, pp. 2307-2309, 1999.

[114] C. Liu, Y. Y. Fan, M. Liu, H. T. Cong, H. M. Cheng and M. S. Dresselhaus, Hydrogen Storage in Single-Walled Carbon Nanotubes at Room Temperature, *Science*, vol. 286, no. 5, pp. 1127-1129, 1999.

[115] G. G. Tibbetts , G. P. Meisner and C. H. Olk, Hydrogen Storage Capacity of Carbon Nanotubes, Filaments, and Vapor-Grown Fibers, *Carbon*, vol. 39, pp. 2291-2301, 2001.

[116] Q. Wang and J. K. Johnson, Molecular Simulation of Hydrogen Adsorption in Single-Walled Carbon Nanotubes and Idealized Carbon Slit Pores, *J. Chem. Phys.*, vol. 110, no. 1, pp. 577-586, 1999.

[117] K.A. Williams and P.C. Eklund, Monte Carlo Simulations of H2 Physisorption in Finite-Diameter Carbon Nanotube Ropes, *Chem. Phys. Lett.*, vol. 320, pp. 352-358, 2000.

[118] S. Maruyama and T. Kimura, Molecular Dynamics Simulation of Hydrogen Storage in Single-Walled Carbon Nanotubes, *Proc. ASME Heat Transfer Division 2000*, Orlando, vol. 2, pp. 405-409, 2000.

[119] Y. Gototsi, J.A. Libera, A.G. Güvenç-Yazicioglu and C.M. Megaridis, In Situ Multiphase Fluid Experiments in Hydrothermal Carbon Nanotubes, *Appl. Phys. Lett.*, vol.79, no 7, pp. 1021-1023,

2001

[120] C. M. Megaridis, A. G. Güvenç-Yazicioglu, J. A. Libera, and Y. Gototsi, Attoliter Fluid Experiments in Individual Closed-End Carbon Nanotubes: Liquid Film and Fluid Interface Dynamics, *Phys. Fluids*, vol.14, no 2, pp. L5-L8, 2002.

[121] E. Dujardin, T. W. Ebbesen, H. Hiura and K. Tanigaki, Capillary and Wetting of Carbon Nanotubes, *Science*, vol. 265, pp. 1850-1852, 1994.

[122] J. H. Walther, R. Jaffe, T. Halcioglou and P. Koumoutsakos, Carbon Nanotubes in Water; Structural Characteristics and Energetics, *J. Phys. Chem. B*, vol.105, pp. 9980-9987, 2001.

[123] T. Werder, J. H. Walther, R .L. Jaffe, T. Halicioglu, F. Noca and P. Koumoutsakos, Molecular Dynamics Simulation of Contact Angles of Water Droplets in Carbon Nanotubes, *Nanoletters*, vol. 1, no 12, pp. 697-702, 2001.

[124] K. Koga, K., G. T. Gao, H. Tanaka and X. C. Zeng, Formation of Ordered Ice Nanotubes inside Carbon Nanotubes, *Nature*, vol.412, pp. 802-805, 2001.

[125] Y. Maniwa, H. Kataura, M. Abe, S. Suzuki, Y. Achiba, H. Kiba and K. Matsuda, Phase Transition in Confined Water inside Carbon Nanotubes, *J. Phys. Soc. Jpn.*, vol. 71, no. 12, pp. 2863-2866, 2002.

[126] S. Maruyama, A Molecular Dynamics Simulation of Heat Conduction of Finite Length SWNTs, *Physica B*, vol. 323, no. 1-4, pp. 193-195, 2002.

[127] S. Maruyama, A Molecular Dynamics Simulation of Heat Conduction of a Finite Length Single-Walled Carbon Nanotube, *Micro. Thermophys. Eng.*, vol. 7, no. 1, pp. 41-50, 2002.

[128] S. Berber, Y.-K. Kwon and D. Tománek, Unusually High Thermal Conductivity of Carbon Nanotubes, *Phys. Rev. Lett.*, vol. 84, pp. 4613-4616, 2000.

[129] S. Lepri, Memory Effects and Heat Transport in One-Dimensional Insulators, *Eur. Phys. J. B*, vol. 18, pp. 441-446, 2000.

[130] R. Livi and S. Lepri, Heat in One Dimension, *Nature*, vol. 421, pp. 327, 2003.

[131] R. Saito, T. Takeya, T. Kimura, G. Dresselhaus and M. S. Dresselhaus, Raman Intensity of Single-Walled Carbon Nanotubes, *Phys. Rev. B*, vol. 57, pp. 4145-4153, 1998.

[132] S. Maruyama, Y. Igarashi, Y. Taniguchi and J. Shiomi, Molecular Dynamics Simulations of Heat Transfer of Carbon Nanotubes, *Micro. Thermophys. Eng.*, to be submitted.

[133] S. T. Huxtable, D. G. Cahill, S. Shenogin, L. Xue, R. Ozisik, P. Barone, M. Usrey, M. S. Strano, G. Siddons, M. Shim and P. Keblinski, Interfacial Heat Flow in Carbon Nanotube Suspensions, *Nature Mat.*, vol. 2, pp. 731-734, 2003.

[134] S. Shenogin, L. Xue, R. Ozisik, P. Keblinski and D. G. Cahill, Role of Thermal Boundary Resistance on the Heat Flow in Carbon-Nanotube Composites, *J. Appl. Phys.*, vol. 95, pp. 8136-8144, 2004.

[135] K. Bolton and S. Gustavsson, Energy Transfer Mechanisms in Gas-Carbon Nanotube Collision, *Chem. Phys.*, vol. 291, pp. 161-170, 2003.

Table 21.1 Parameters for Lennard-Jones potential for inert gas molecules.

	σ [nm]	ε [J]	ε/k_B [K]
Ne	0.274	0.50×10^{-21}	36.2
Ar	0.340	1.67×10^{-21}	121
Kr	0.365	2.25×10^{-21}	163
Xe	0.398	3.20×10^{-21}	232

Table 21.2 Reduced properties for Lennard-Jones system.

Property		Reduced Form
Length	$r^* =$	r/σ
Time	$t^* =$	$t/\tau = t(\varepsilon/m\sigma^2)^{1/2}$
Temperature	$T^* =$	$k_B T/\varepsilon$
Force	$f^* =$	$f\sigma/\varepsilon$
Energy	$\phi^* =$	ϕ/ε
Pressure	$P^* =$	$P\sigma^3/\varepsilon$
Number density	$N^* =$	$N\sigma^3$
Density	$\rho^* =$	$\sigma^3\rho/m$
Surface tension	$\gamma^* =$	$\gamma\sigma^2/\varepsilon$

Table 21.3 Potential parameters for water.

		SPC/E	TIP4P
r_{OH}	[nm]	0.100	0.095 72
∠HOH	[°]	109.47	104.52
σ_{OO}	[nm]	0.316 6	0.315 4
$\varepsilon_{OO} \times 10^{-21}$	[J]	1.079 7	1.077 2
r_{OM}	[nm]	0	0.015
q_H[a]	[C]	0.423 8 e	0.52 e
q_M	[C]	-0.847 6 e	-1.04 e

[a]Charge of electron e = 1.60219×10^{-19} C

Table 21.4 Parameters for Tersoff potential and Brenner potential.

	Tersoff (Si)	Tersoff (C)	Brenner (C)
D_e [eV]	2.6660	5.1644	6.325
R_e [nm]	0.2295	0.1447	0.1315
S	1.4316	1.5769	1.29
β [nm^{-1}]	14.656	19.640	1.5
A	1.1000×10^{-6}	1.5724×10^{-7}	1.1304×10^{-2}
N	7.8734×10^{-1}	7.2751×10^{-1}	1
δ	1/(2n)	1/(2n)	0.80469
c	1.0039×10^{5}	3.8049×10^{4}	19
d	1.6217×10^{1}	4.384	2.5
h	-5.9825×10^{-1}	-5.7058×10^{-1}	-1
R [nm]	0.285	0.195	0.185
D [nm]	0.015	0.015	0.015

Table 21.5 Calculation conditions of contact of Lennard-Jones fluid.

		Droplet		Bubble	
	ε^*_{SURF}	ε_{INT} [10^{-21}J]	θ [deg]	ε_{INT} [10^{-21}J]	θ [deg]
E0	0.73	0.228	-	-	-
E1	1.29	0.404	135	-	-
E2	1.86	0.581	110	0.527	101
E3	2.43	0.758	79	0.688	69
E4	2.99	0.935	49	0.848	23
E5	3.56	1.112	-	1.009	-

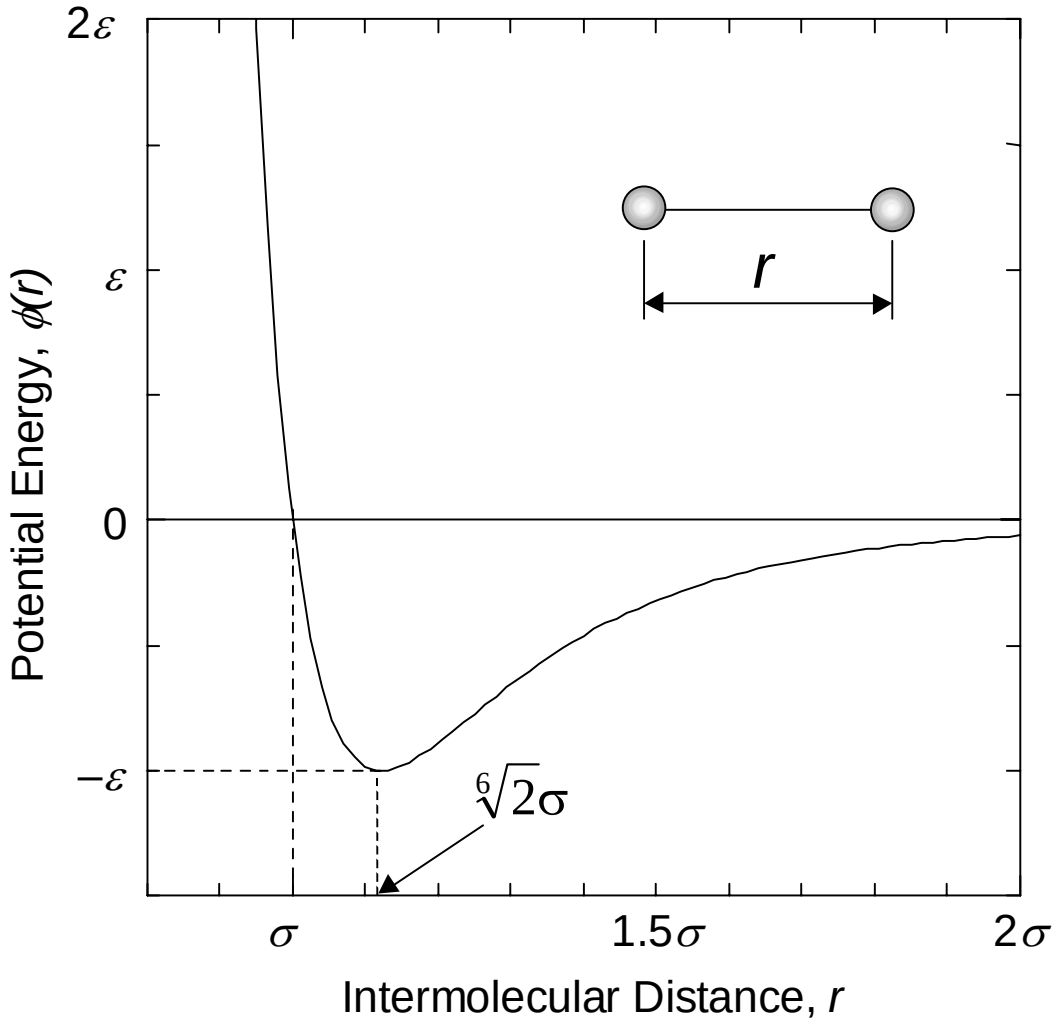

Figure 21.1. Lennard-Jones (12-6) potential.

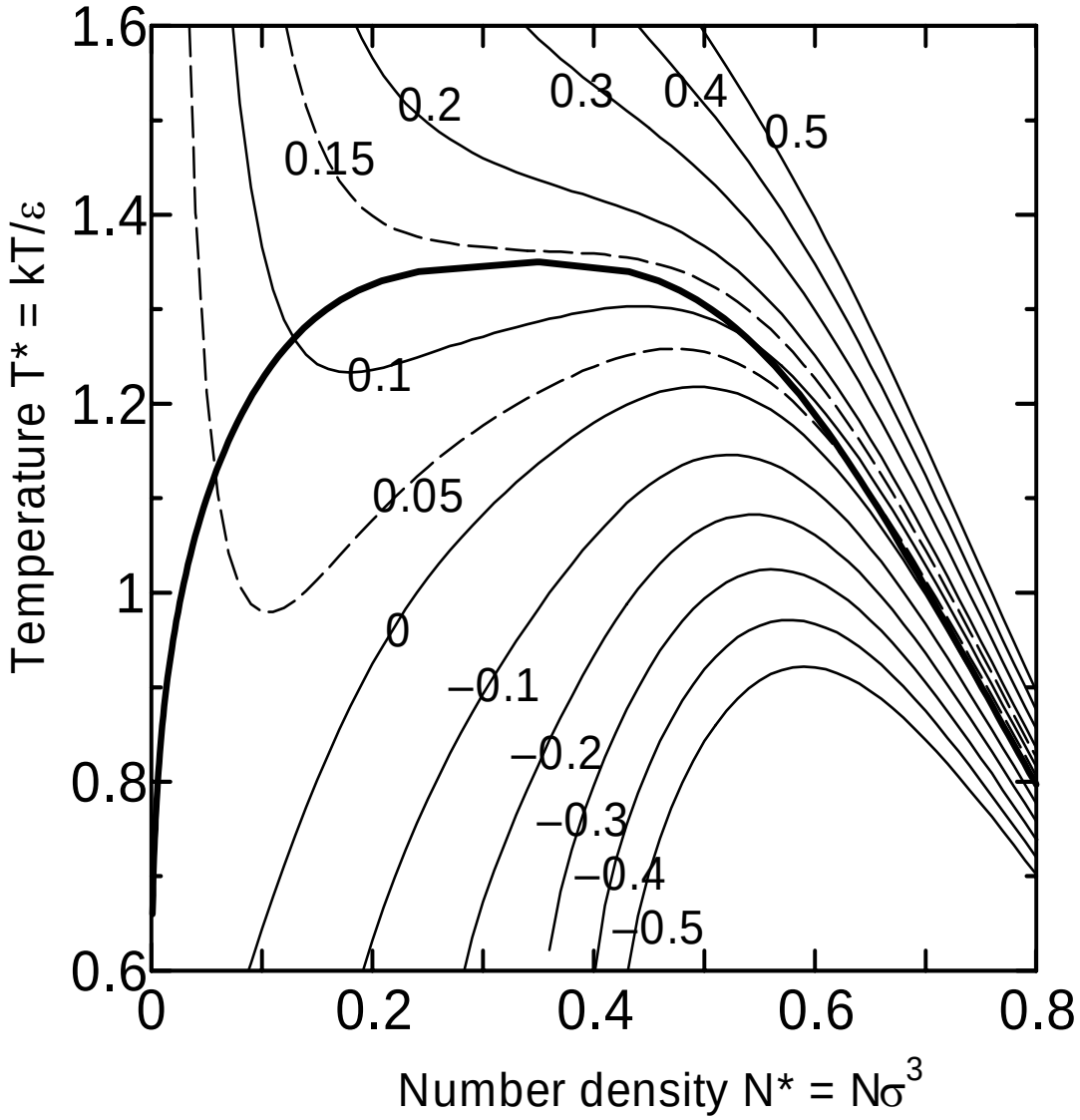

Figure 21.2. Phase diagram of Lennard-Jones fluid based on the equation of state by Nicolas et al.

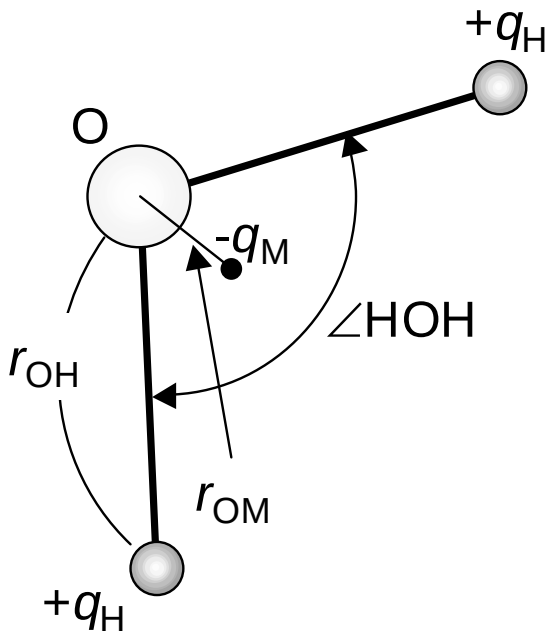

Figure 21.3. Classical rigid models of water for 4-sites and 3-sites models, TIP4P, CC, SPC/E.

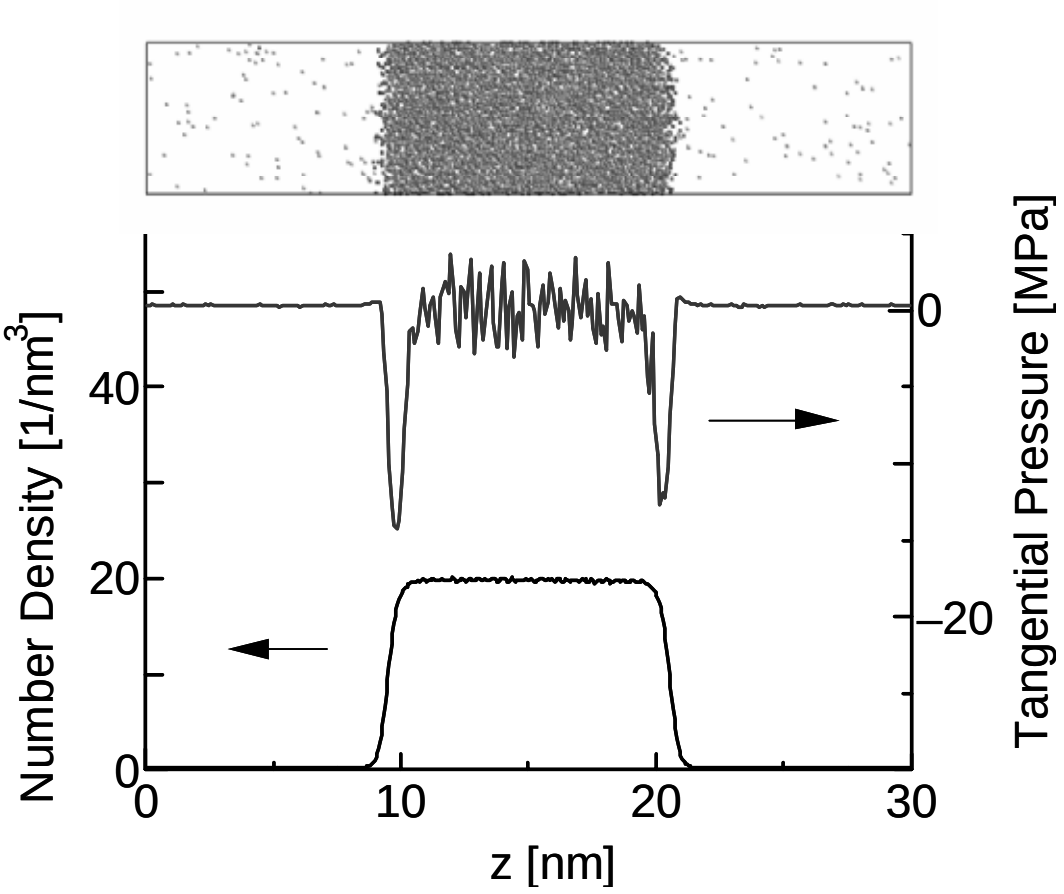

Figure 21.4. Density and tangential pressure distribution of a flat liquid-vapor interface (8000 argon molecules saturated at 99.5 K in 6×6×30 nm box).

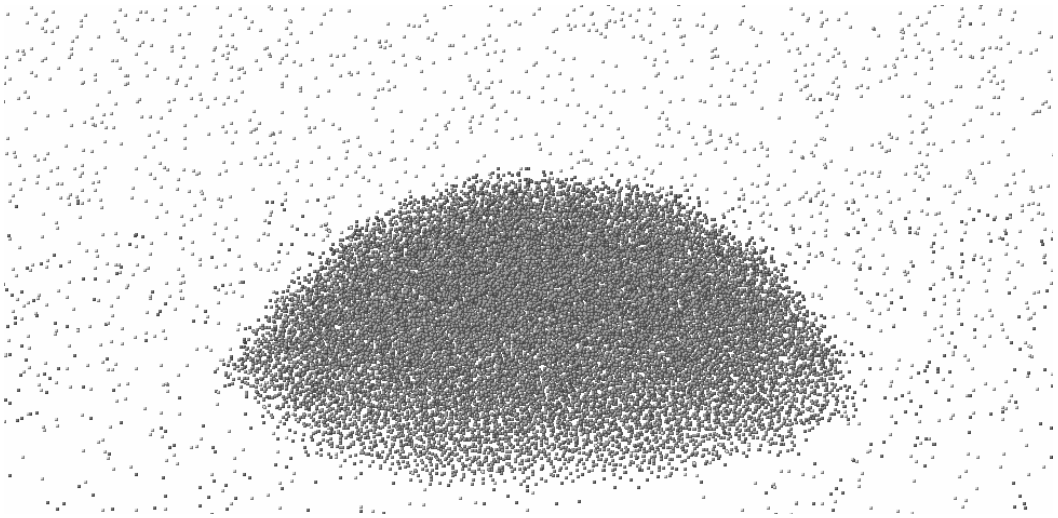

(a) snapshot

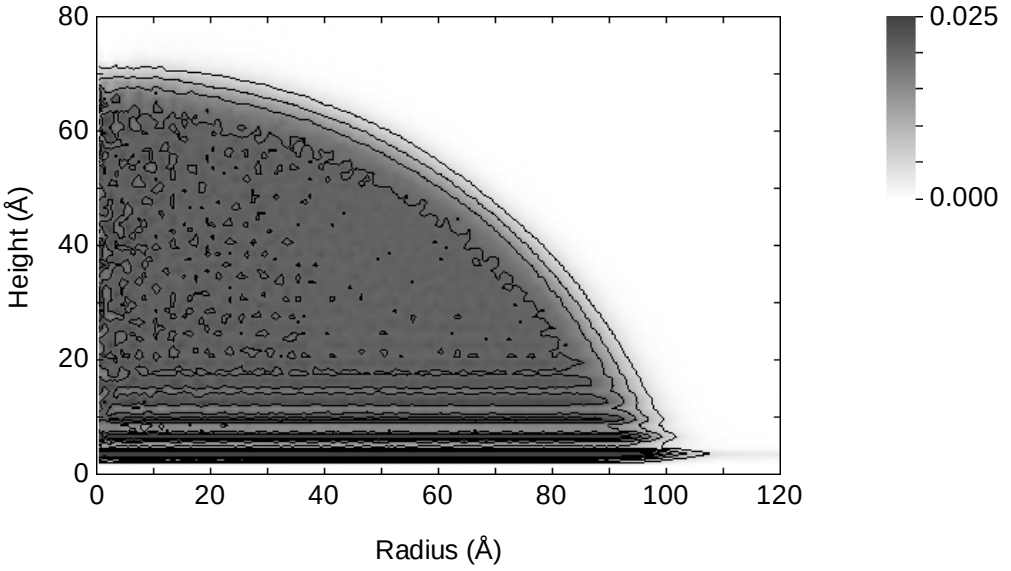

(b) Density profile

Figure 21.5. A snapshot of a liquid droplet on solid surface compared with the two-dimensional density profile: 32000 Lennard-Jones molecules on a surface.

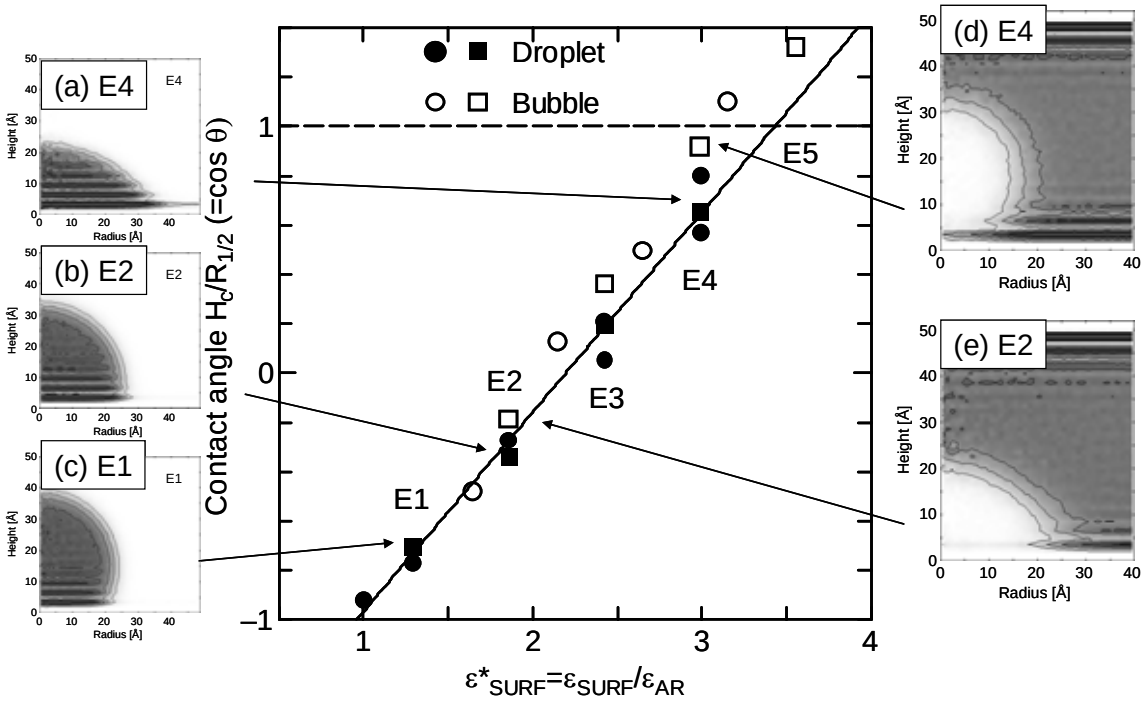

Figure 21.6. Dependence of contact angle on the integrated depth of surface potential. Inserted are two dimensional density distributions for droplets (a-c) and for bubbles (d,e).

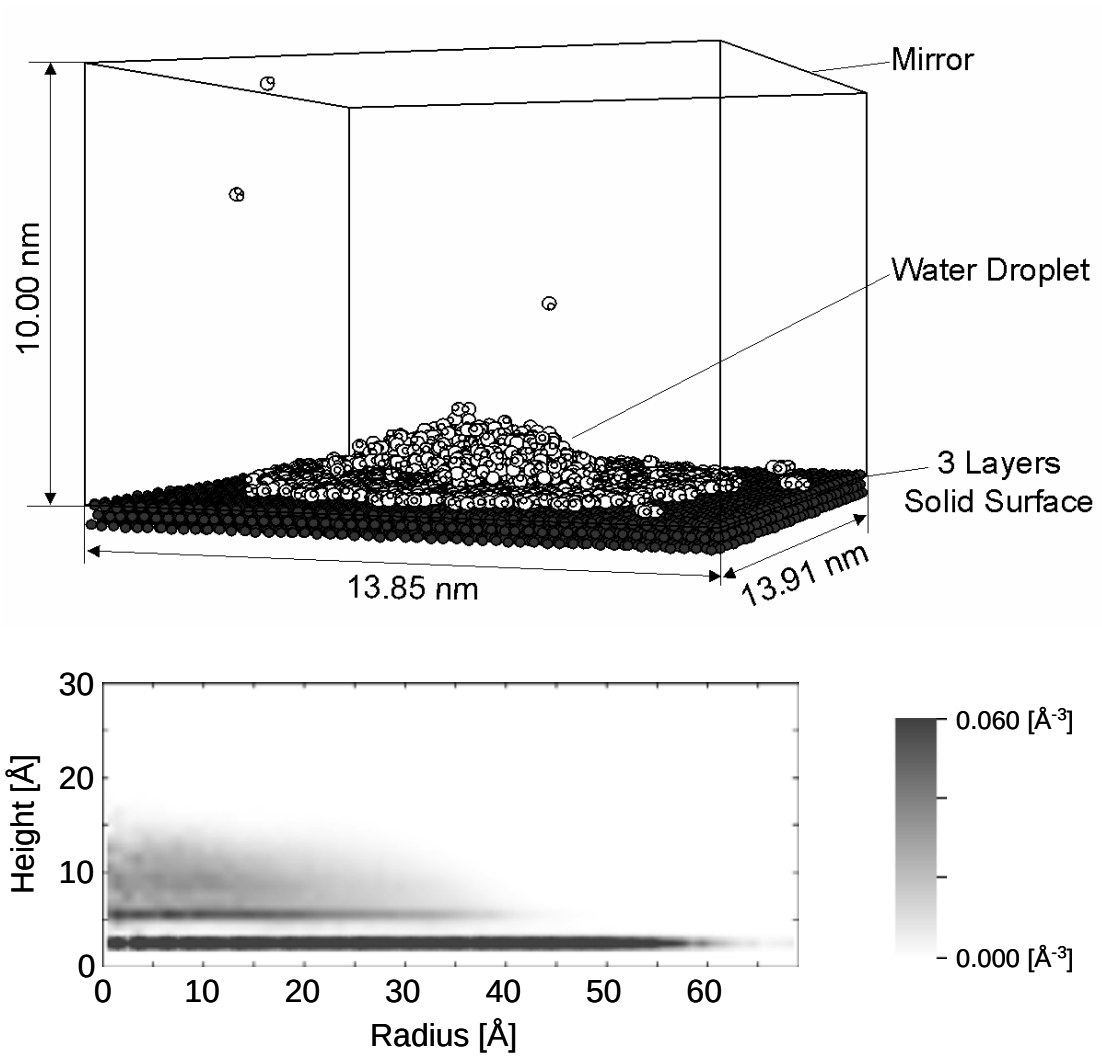

Figure 21.7. A snapshot and 2-dimensional density profile of an equilibrium water droplet on a platinum surface at 350K. SPC/E water molecules were interacting with the harmonic platinum surface represented by 3 layers of (111) surface through the water-platinum potential proposed by Zhu-Philpott.

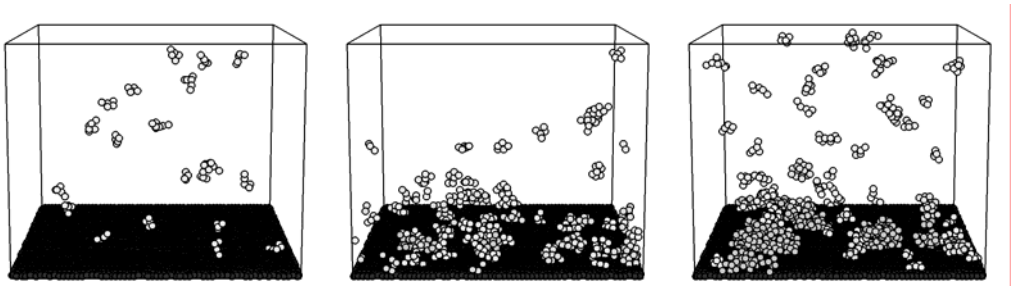

(a) 500 ps (b) 1000 ps (c) 1500 ps

Figure 21.8. Nucleation of liquid droplet on a solid surface. Only clusters larger than 5 atoms are displayed for clarity.

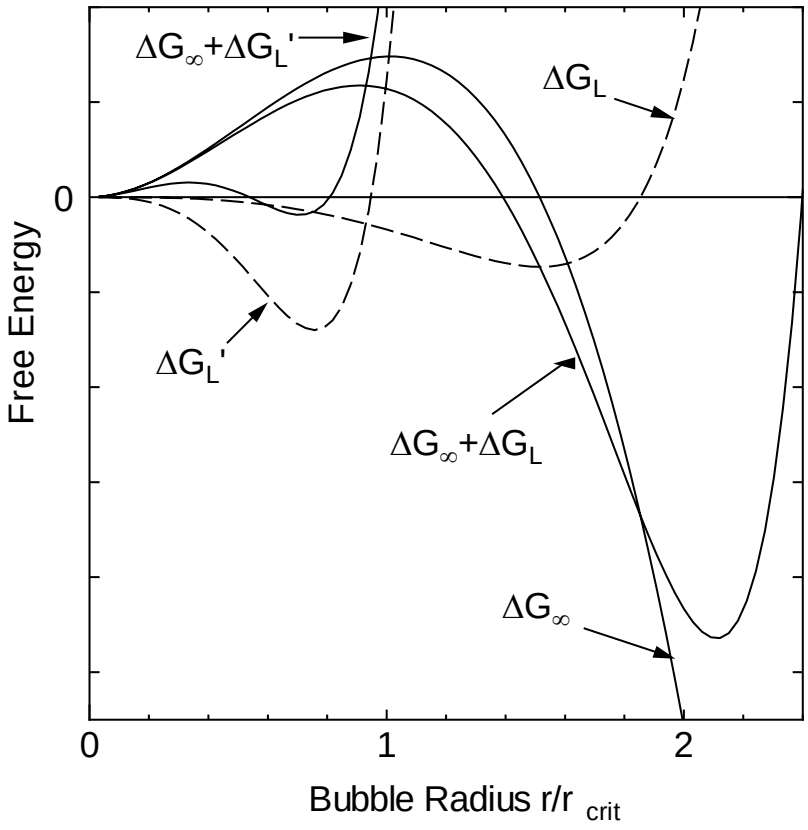

Figure 21.9. Modification of free energy for a confined nano-bubble.

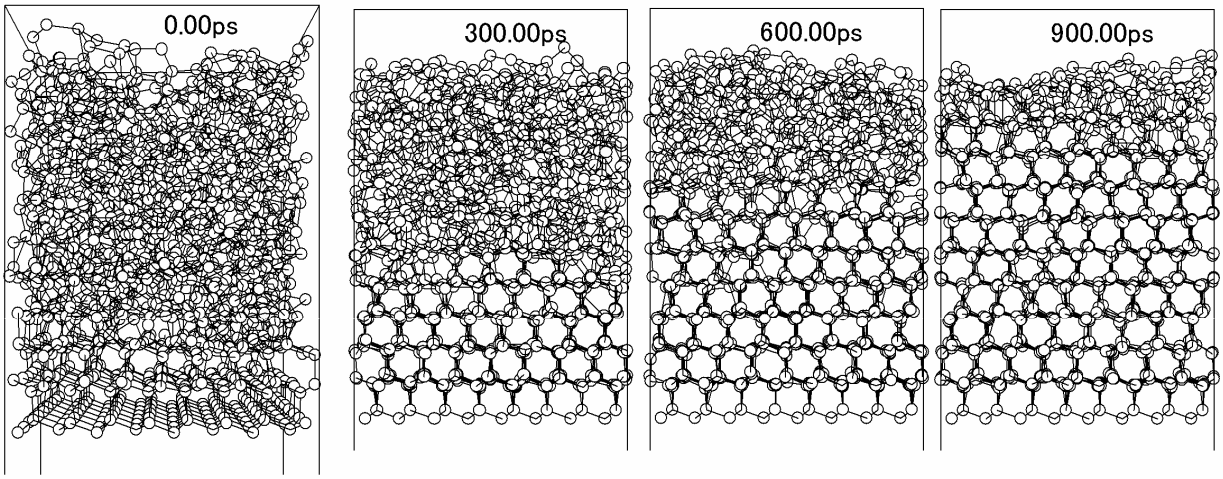

Figure 21.10. Snapshots of Solid Phase Epitaxy (SPE) growth of silicon crystal in (111) at 2100K.

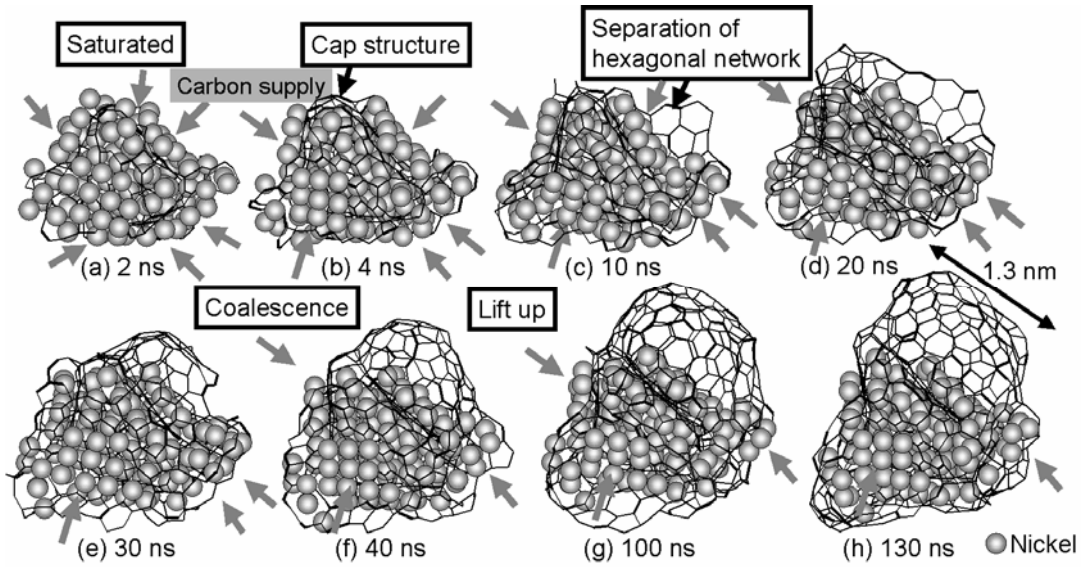

Figure 21.11. Snapshots of the catalytic CVD growth process of the cap structure of an single-walled carbon nanotube. Gray circles represent nickel atoms. Carbon atoms are not shown for clarity. Gray arrows show a typical supply route of carbon atoms from expose metal surface.

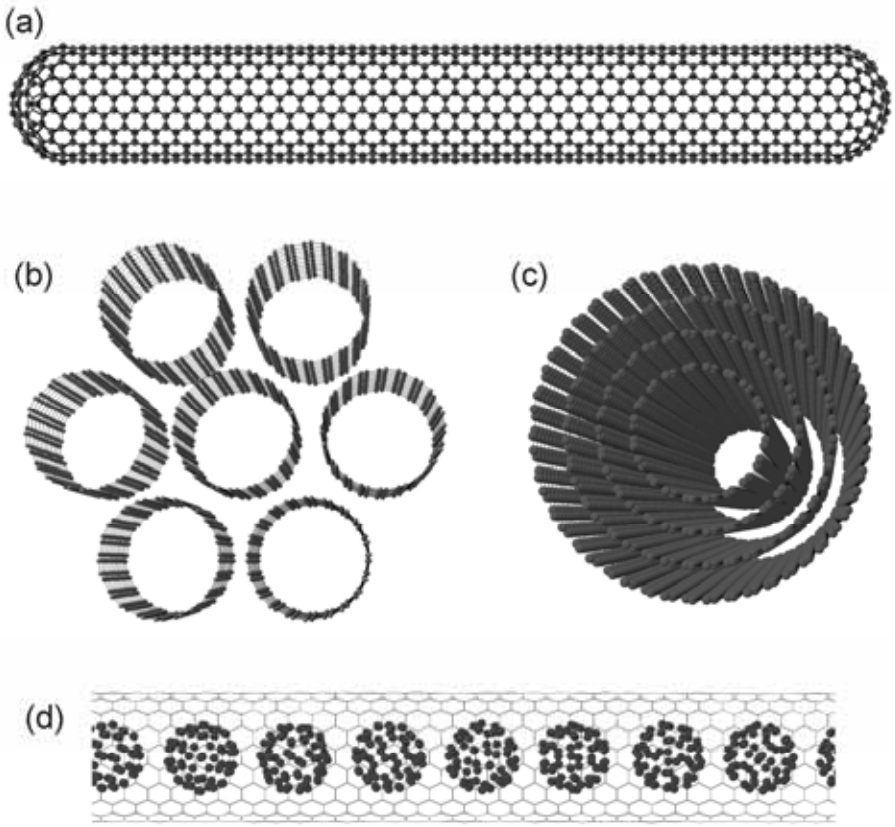

Figure 21.12. Geometrical structure of carbon nanotubes. (a) Single-walled carbon nanotube (SWNT) with (10, 10) chirality. (b) A bundle of SWNTs. (c) Multi-walled carbon nanotube (MWNT). (d) Peapod: nanotube filled with fullerenes.

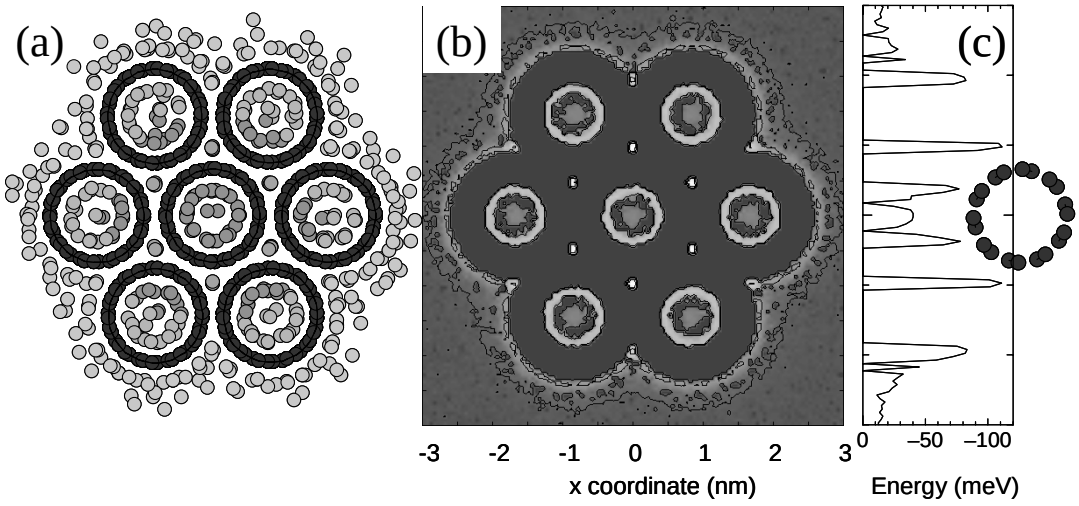

(a) (b)

Figure 21.13. Physisorption of hydrogen in a bundle of single-walled carbon nanotubes at 77K. (a) A snapshot, (b)(c) potential energy distribution.

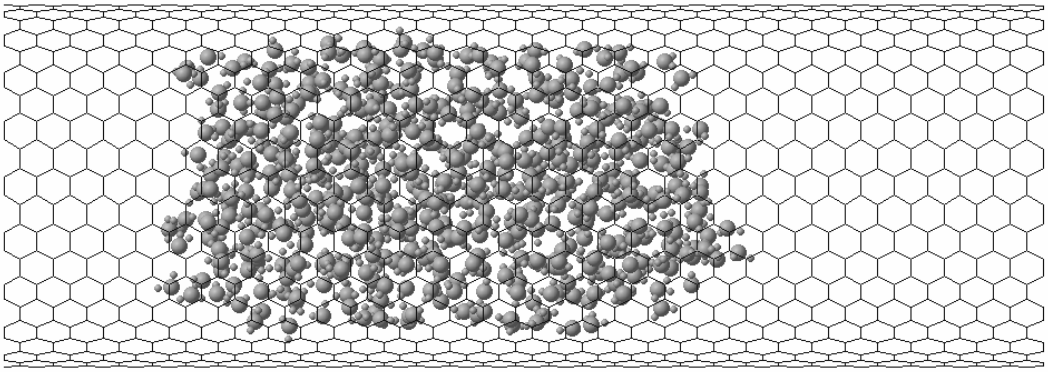

Figure 21.14. Structure of a water cluster in a carbon nanotube. (512 water molecules in (20, 20) nanotube with 2.77 nm diameter).

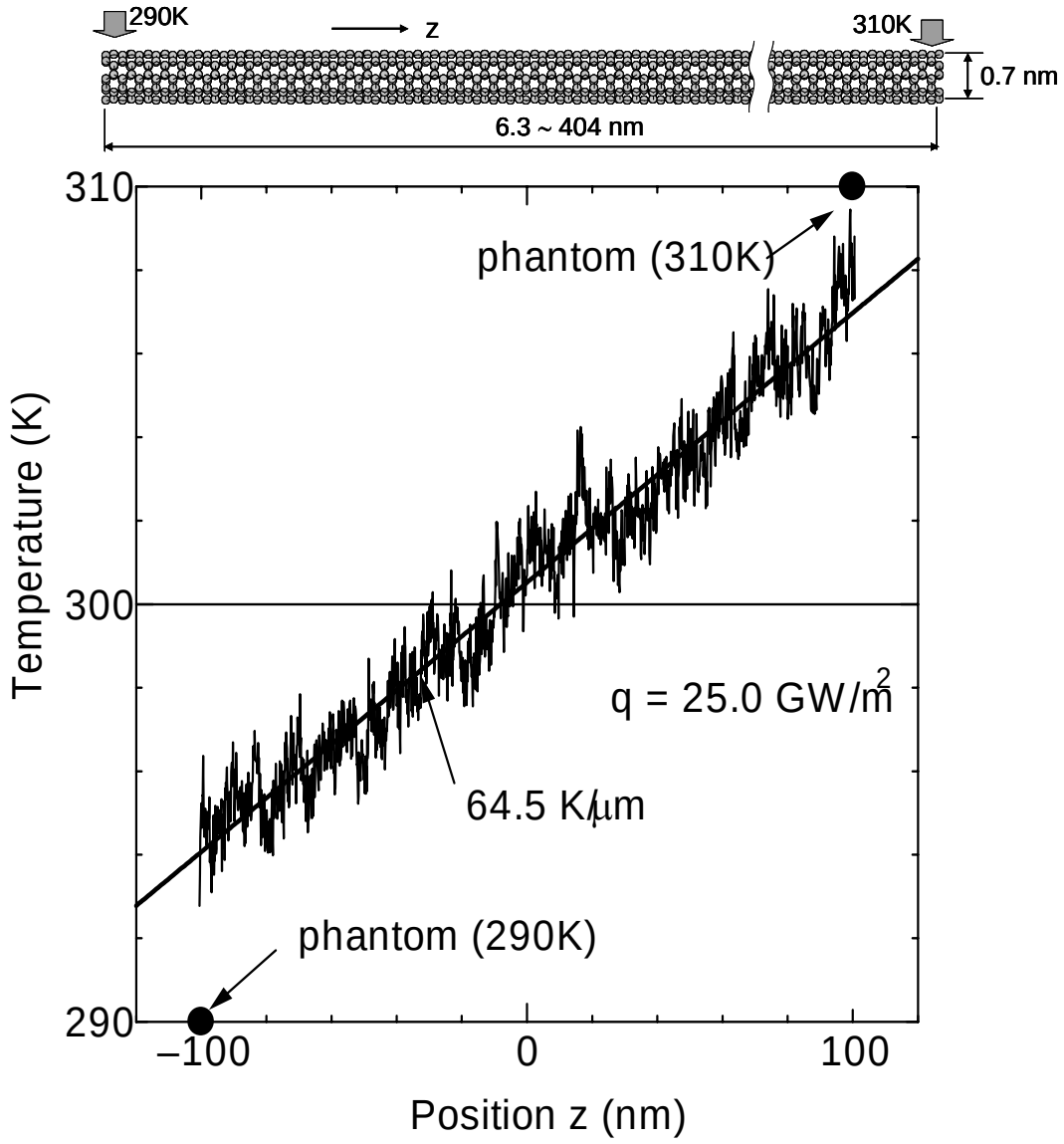

Figure 21.15. Molecular dynamics simulation of heat conduction along a single-walled carbon nanotube. Temperature distribution along a nanotube with (5, 5) chirality and 202 nm in length.

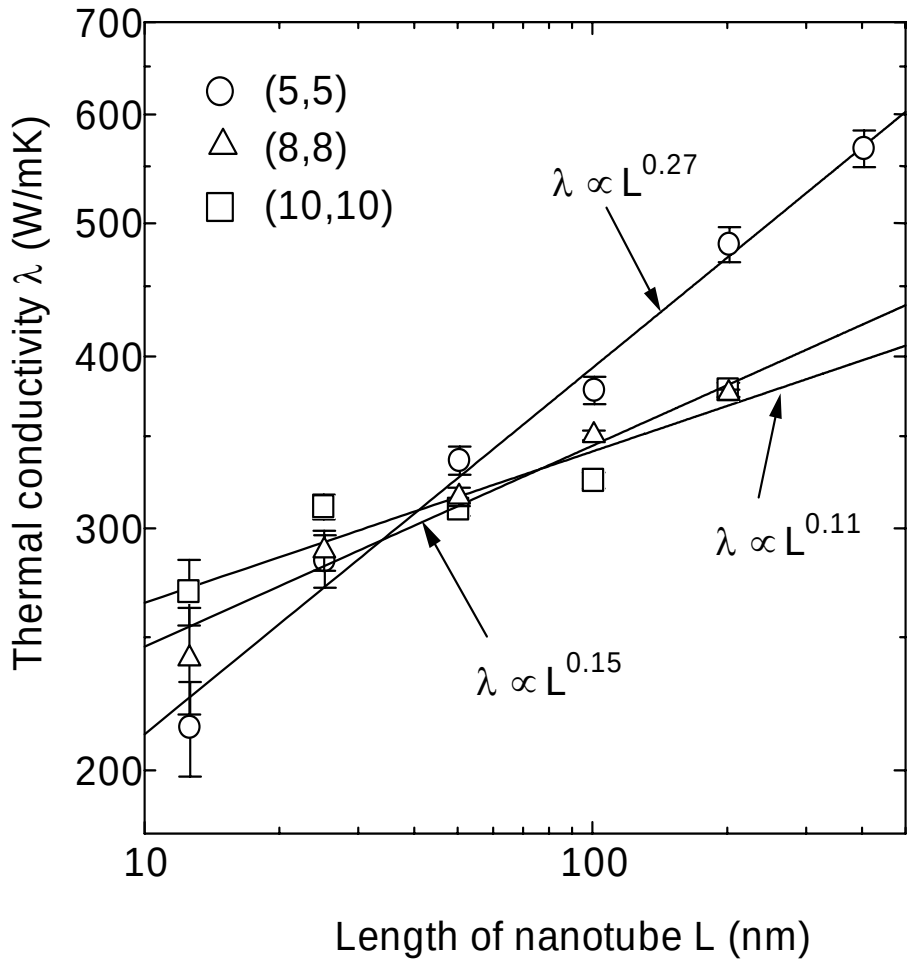

Figure 21.16. Dependence of thermal conductivity on length of nanotubes for 300K.

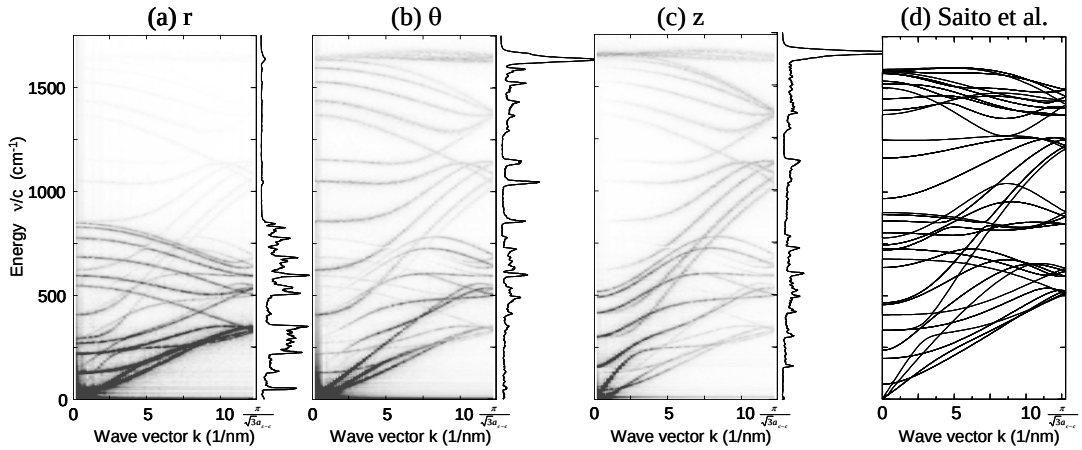

Figure 21.17. Phonon dispersion relation and photon density of states for 101 nm long (5, 5) SWNT. Dispersion relations from r, θ and z components of displacement are shown in (a), (b) and (c) respectively. The phonon density of states calculated as power spectra of v_r, v_θ, v_z are shown as the right hand side of each dispersion relation. (d) The dispersion relations solved from the dynamical matrix using the force-constant tensor scaled from those for 2D graphite.

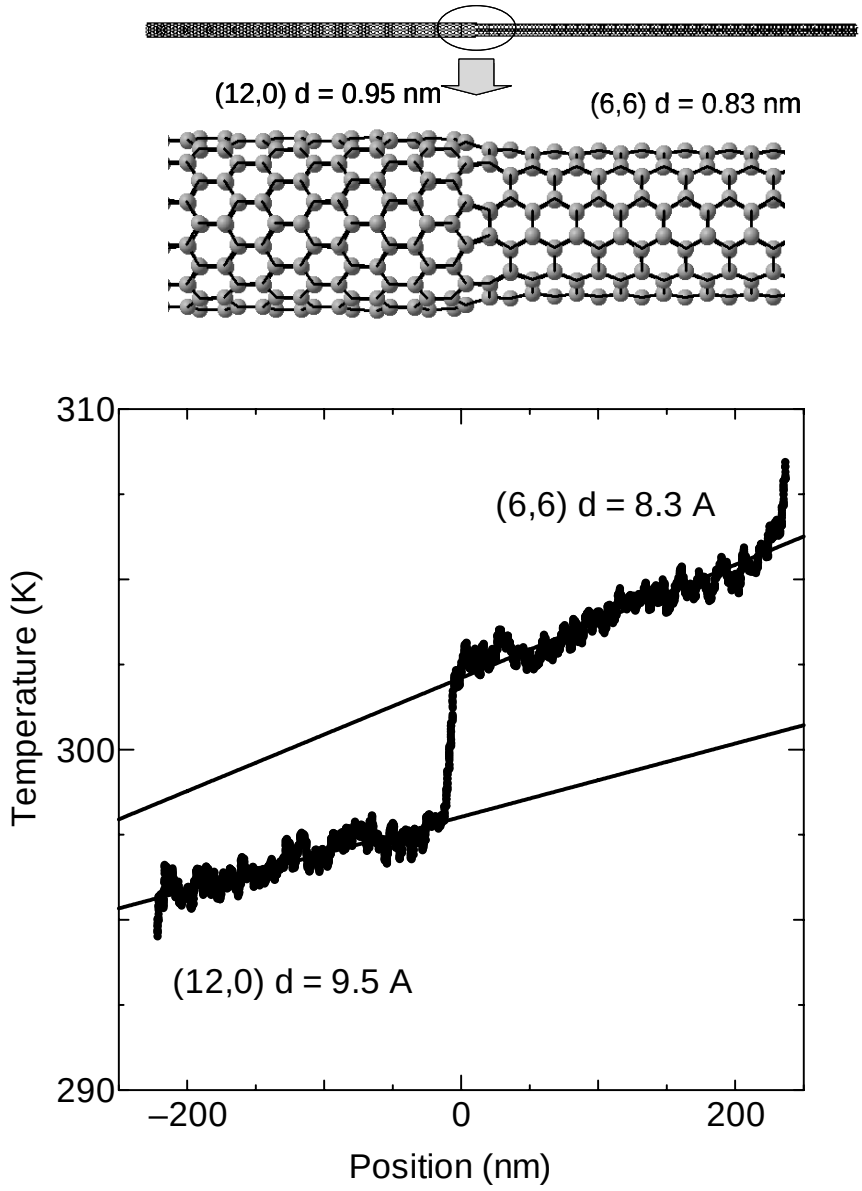

Figure 21.18 Temperature jump and thermal boundary resistance at a junction of single-walled carbon nanotubes.

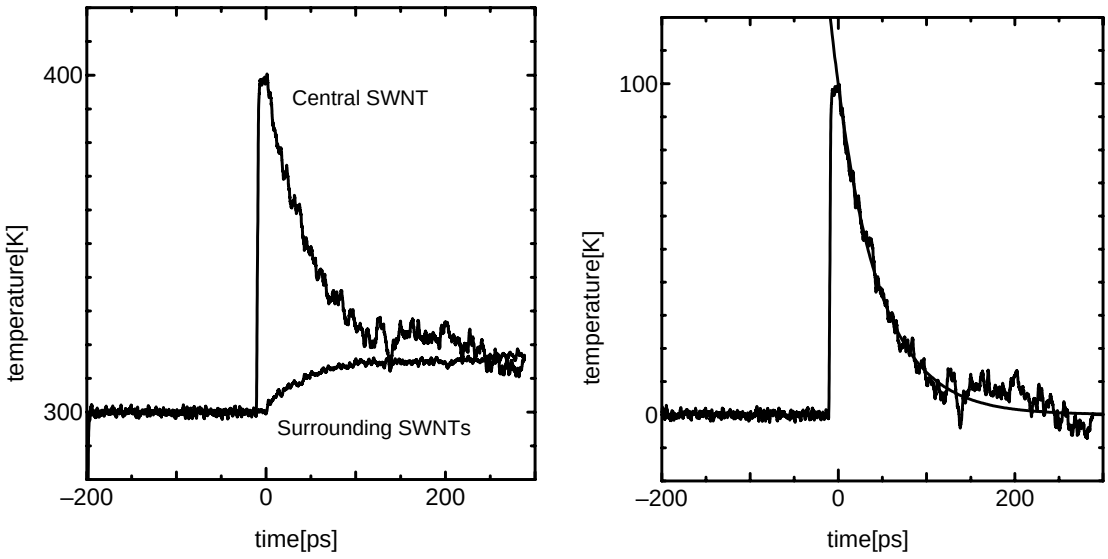

(a) (b)

Figure 21.19 Measurement of the thermal boundary resistance between single-walled carbon nanotubes in a bundle. (a) Time histories of the temperature of hot (central) SWNT and cold (surrounding) SWNTs. (b) Time history of the temperature difference.